Stockholm University

Master Thesis

Degree Project in
Geology, 60 hp

Metamorphic Evolution of the Rechnitz Window (Eastern Alps)

Gregor Karl Weltz

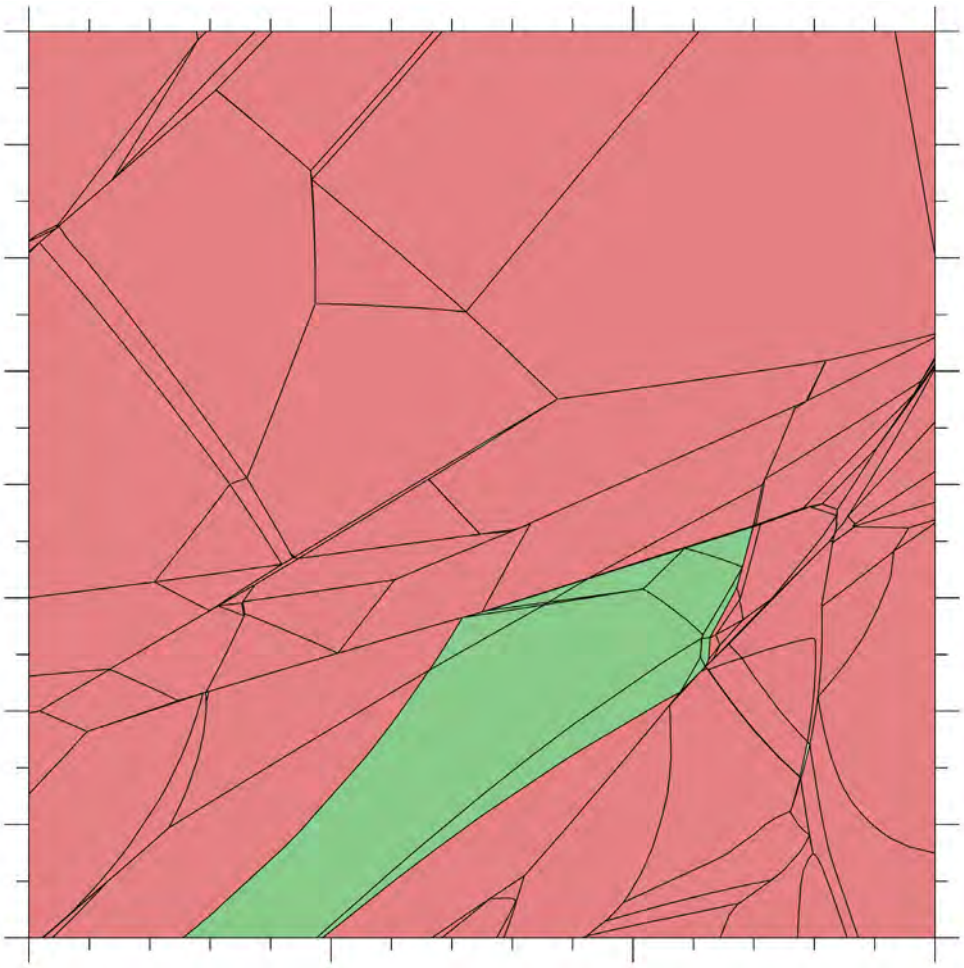

Stockholm 2026

Department of Geological Sciences
Stockholm University
SE-106 91 Stockholm

Abstract

This thesis aims to reconstruct the Alpine metamorphic evolution of the Rechnitz Window in the Eastern Alps. Petrographic observations, whole-rock and mineral geochemistry were conducted on metabasalts and plagiogranites. In addition, for the first time, thermodynamic modelling was applied to the Rechnitz Window to estimate the peak pressure-temperature conditions recorded by a metamorphosed plagiogranite that contains abundant blue amphibole (riebeckite and Fe-glaucophane) and albite. Calculations were performed using the amount of FeO and Fe_2O_3 measured in the bulk rock. Peak pressure-temperature conditions of ~4-6.5 kbar and 395-460°C were estimated for the Rechnitz Window.

1 Introduction

Many geologists associate the occurrence of blue amphiboles, such as glaucophane and riebeckite, the index minerals of the blueschist facies, with specific pressure-temperature (P-T) conditions. Most textbooks report broad blueschist P-T values between 6-16 kbar and 100-550°C (Winter, 2014) or 8-20 kbar and 150-550°C (Bucher and Grapes, 2011). Thus, the occurrence of blueschist serves only as a rough proxy for estimating P-T conditions during oceanic subduction.

The Alps, formed through the closure of the Tethys Sea caused by the convergence of the European and African-Adriatic plates (Le Breton et al., 2021), make an excellent study area for blueschists. In the Rechnitz Window, the easternmost and lesser-researched Penninic Window in the Alps, detailed P-T analyses have been performed. Researchers such as Koller (1985) constrained the P-T conditions to 330-370°C and 6-8 kbar for an older metamorphic event, and 390-430°C and <3 kbar for a younger metamorphic event, using mineral paragenesis. More recently, a group of students at the Freie Universität Berlin (hereafter referred to as the Berlin group, whose work remains unpublished) used Raman spectroscopy on carbonaceous material, concluding a T_{max} of 422°C in the Rechnitz Window. The above-cited P-T estimates by Koller (1985) do not consider whole-rock chemistry, which is key to understanding the formation of sodic amphibole, especially at the greenschist-blueschist boundary. This is because studies such as Manzotti et al. (2020) and Diener and Powell (2010) show that the growth of sodic amphibole is strongly influenced by the rock's chemical composition. Ratios such as Fe^{2+}/Fe^{3+} or the rock's Na content can facilitate or hinder the growth of sodic amphibole, even at otherwise favourable conditions.

One method for estimating P-T conditions that accounts for bulk-rock geochemistry is thermodynamic modelling, specifically the calculation of pseudosections. A pseudosection defines stable mineral assemblages over a specific P-T space for a given bulk rock chemical composition. For the first time ever in the Rechnitz Window, a pseudosection is constructed to estimate the peak Alpine P-T conditions recorded by a metamorphosed plagiogranite.

The data obtained in this thesis are used to critically discuss (i) the role of the bulk rock composition (especially the whole-rock Fe^{2+}/Fe^{3+} ratio) on the stability field of blue amphibole and (ii) the uncertainties and limits of thermodynamic modelling applied to rocks that display high Fe^{2+}/Fe^{3+} ratios.

2 Geologic Setting

2.1 The Piemont-Liguria Ocean in the Alps

The Piemont-Liguria Ocean, part of the Alpine Tethys, was an ocean situated between the European plate to the north and the African-Adriatic plate to the south. At its widest, it was 300 km across. It formed through the divergence of the European plate and the south-westward-moving African plate starting in the Early-Middle Jurassic following the breakup of Pangea (Froitzheim et al., 1996; Le Breton et al., 2021). This passive rifting process was driven by externally applied forces from the velocity difference between the African and European plates, rather than by thermal processes such as a mantle plume. The early rifting was slow, at only 5mm/year, but sped up towards the Middle Jurassic, reaching 20 mm/year. Eventually, after around 10 My, upwelling of magma with normal-MOR composition filled chambers, forming olivine-, as well as Fe-Ti-gabbros (Hoogerduijn-Strating, 1991). During the Middle Jurassic, the first oceanic crust formed, and deep-marine radiolarites were deposited above it and along the continental margins (Le Breton et al., 2021). Ages of 166-160 Ma are reported (Rosenbaum & Lister, 2005).

The first stage of closure began in the Late Cretaceous with the opening of the Atlantic, which led to a counterclockwise rotation of the African plate, shifting extensional forces toward a compressional regime and initiating the formation of a subduction zone within the Piemont-Liguria Ocean. This subduction began in the most internal parts of the Ocean, leading to the formation of an interoceanic accretionary wedge and subjecting rocks at depth to eclogite-facies conditions. This process continued throughout the Cretaceous with progressing accretion and westward nappe stacking (Hoogerduijn-Strating, 1991; Schmid et al., 2004). The second stage of the closure corresponds to the continental collision of the Piemont-Liguria Ocean and the European plate and was controlled by the acceleration of the African plate towards the European plate (Hoogerduijn-Strating, 1991). The collision itself started at the Adriatic margin around 84 Ma and progressed SE-NW across the Piemonte-Liguria Ocean and neighbouring units. Lastly, the remaining oceanic domains were consumed during the later Apennine rollback subduction 35 Ma, marking the final stages of Alpine Tethys closure. (Le Breton et al., 2021). A detailed illustration of the steps described above by Le Breton et al. (2021) is shown in Figure 1 below. The authors note uncertainty regarding the eastern extent and timing of the ocean's closure, indicated by “?” for the eastern extent of the Piemont-Liguria ocean.

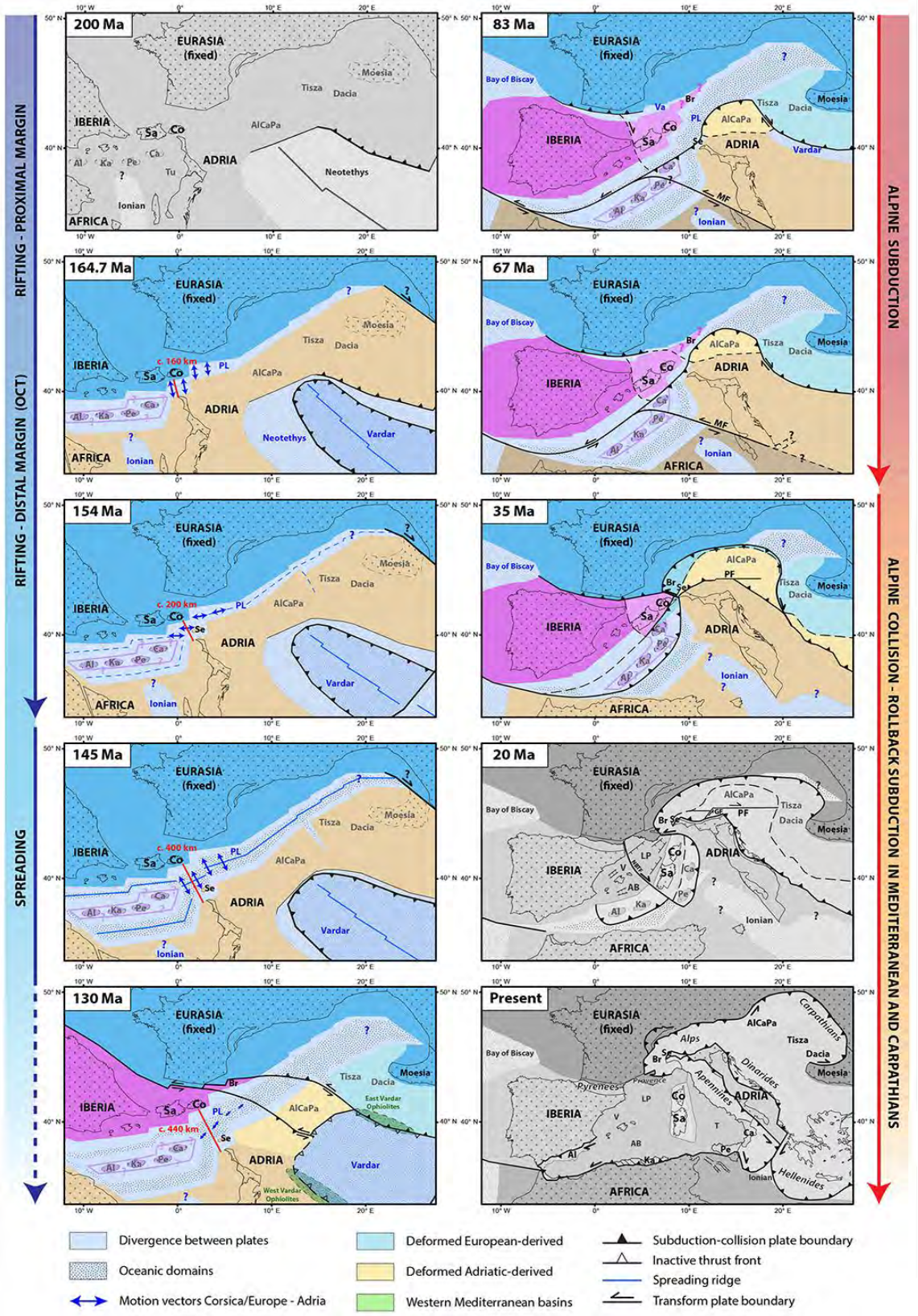

Figure 1: Tectonic map of the evolution of the Western Mediterranean-Alpine, modified from Le Breton et al. (2021). Here, the abbreviation PL stands for Piemont-Liguria, both the ocean and the basin, and is highlighted in pale blue with black dots. Tectonic stages in grey-scale are less relevant to this thesis.

2.2 The Rechnitz Window in the Eastern Alps

The Piemont-Liguria ophiolites, together with the Briançonnais and the Sesia-Dent Blanche, form the Penninic Front (Ballèvre et al., 2018). The Rechnitz Window, together with the Bernstein, Möltern, and Eisenberg Windows, is one of the four Penninic units in the Eastern Alps, collectively referred to as the Rechnitz series, and is placed below the Austroalpine nappes (see Figure 2). On a large scale, the series hosts mainly oceanic sediments, metamorphic limestones, and calc- and quartz phyllites. Ultramafites, metagabbros and greenschists are less common (Ratschbacher et al., 2004). The Rechnitz Window comprises two tectonic units separated by a ductile thrust fault (Cao et al., 2013; Marton et al., 1987); the lower unit consists of Mesozoic sediments, while the upper unit is a Cordilleran-style metamorphic core complex (MCC). The lower unit mainly hosts calcareous and quartz phyllites, while the upper unit consists of greenschists, ophiolite remnants and rarely blueschists. The Rechnitz Window, being an MCC, hinges on observations that the early metamorphism of the Penninic units is not visible on the overriding Austroalpine units, suggesting that a fault separates them, and on the fault geometry in relation to neighbouring units (Cao et al., 2013).

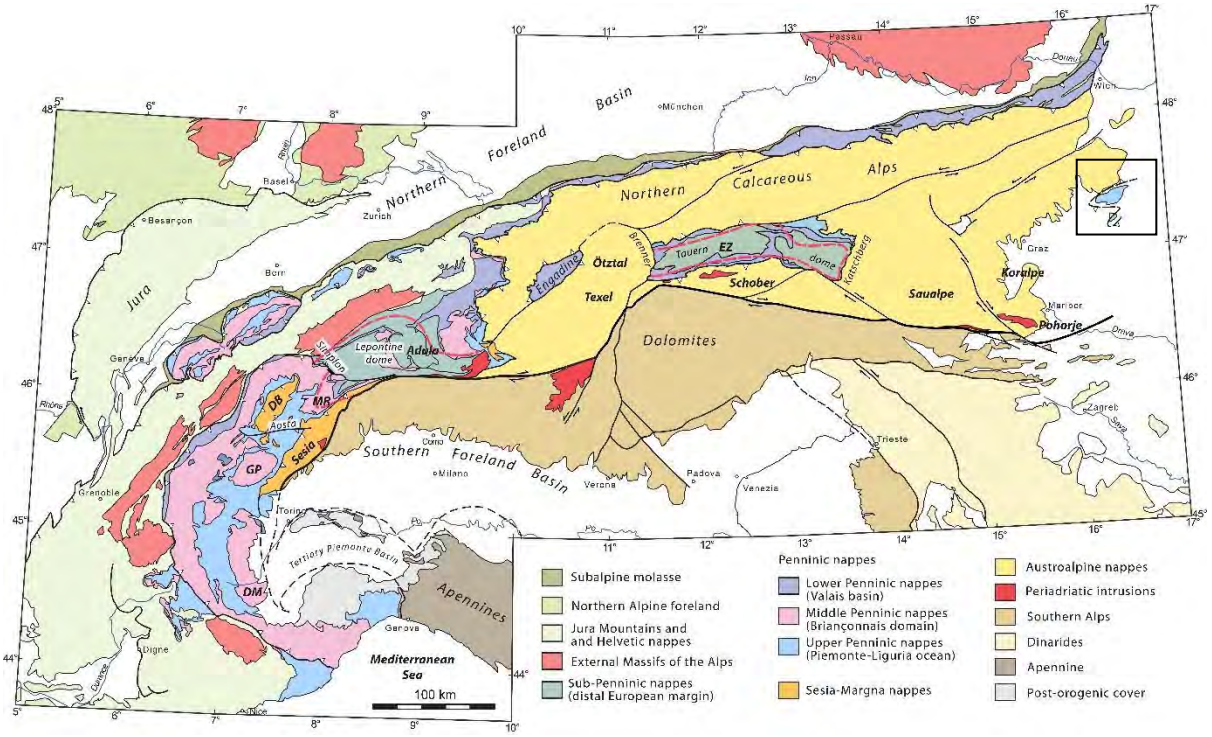

Figure 2: Tectonic map of the Alps (from Manzotti and Ballèvre 2024). The Rechnitz Window (black rectangle, top right) crops out in the Eastern Alps as a window below the Austroalpine nappes.

Three metamorphic stages are described in the Rechnitz Window.
The first stage predates Alpine history, while the other two are associated with Alpine evolution. Based on several amphiboles (barrosite, pargasite and Mg-hornblende), pre-subduction oceanic metamorphism (i.e., the first metamorphic stage) can be constrained to 500 °- 750 °C, while reactions below 500° cannot be discerned due to Alpine overprint (Marton et al., 1987).

The second stage, high-pressure Alpine metamorphism, K/Ar-dated at 65±5 Ma in zoned Crossite-Riebeckite, is constrained by the mineral assemblage acmite, crossite, hematite, magnetite, and albite at 330°-370 °C and 6-8 kbar, though higher pressures are possible. This pressure corresponds to 15-25 km subduction depth and a low thermal gradient (Koller 1985, Marton et al., 1987).
Lastly, the third metamorphic stage is associated with the growth of acmite, biotite, chlorite, epidote, apatite and titanite. It occurred at <3kbar at 390°-430°C during exhumation of the Rechnitz Window, K/Ar dating in micas results in 19-22 Ma. Greenschist-facies metamorphism frequently overprinted the two previous metamorphic stages.

An investigation by Cao et al. (2013) into the structures and microfabrics of the upper unit identified the deformation stages (D) outlined below.

1) D_1 is associated with the development of a weak foliation, marked by fine-grained blue amphiboles
2) D_2 is associated with the development of the S_2 foliation and lineation fabrics of annealed, greenschist overprinted minerals and formed during nappe stacking
3) D_3 results in the development of a penetrative S_3 foliation outlined by asymmetric feldspar porphyroblasts, layers of recrystallised quartz and mica orientation
4) D_4 is the final stage of ductile deformation and is associated with folding.

3 Methods

3.1 Petrography

Thin sections were studied by optical microscopy, in plane and crossed polarised light (hereafter referred to as PPL and XPL, respectively). Microscopic observations were performed using a Leica DLMS series microscope and recorded using the LasEZ software with a Leica MC170HD camera at a maximum resolution of 2592x1944 pixels. Exposure, gamma, contrast, and saturation were manually adjusted to most closely match the colours seen through the microscope. Some images were focus-stacked to compensate for the shallow depth of field. This was achieved by taking several images with slightly different focus distances but the same exposure settings. After that, images were loaded in Adobe Photoshop and aligned using the auto-align tool (though this is only a precautionary step, as the thin section is not moved between images). Finally, the auto-blending tool was used with the “stacking” setting enabled. This process increases the images’ contrast. To compensate for this, images shot for focus stacking were taken with intentionally lower contrast settings.

3.2 Point Counting

To facilitate comparison across domains, modal mineral abundance was estimated. Instead of traditional point counting, digital image analysis (using software such as Adobe Photoshop) is an excellent alternative that offers a degree of automation. However, only a few researchers have applied this method. For instance, Zhang et al. (2014) estimated the surface occupied by pore spaces in a rock using this approach. Here, they are manually selected areas of interest (i.e. the pore spaces). By contrast, an automated approach was applied in this thesis as explained below.

Three images were taken with the LasEZ software: one overexposed in PPL, one underexposed in PPL, and one with high saturation or regular exposure in PPL. These images were loaded on individual layers in Adobe Photoshop. Firstly, the overexposed image was used to manually overpaint all black tones, thereby highlighting only the opaque minerals. This can be done automatically by selecting all black tones using the "colour selection" tool, as, in an overexposed image, only opaques will be black. When needed, the selection can be adjusted manually. All highlighted pixels are then overpainted on a new layer to later allow for automatic pixel counting. Secondly, the underexposed image was used to colour-select and overpaint all white areas, thereby highlighting only feldspar and quartz in this sample. The selection was adjusted using the "expand selection" tool. For the samples in this thesis, a two-pixel expansion was used (see Figure 3). Again, selected pixels are overpainted in a new layer.

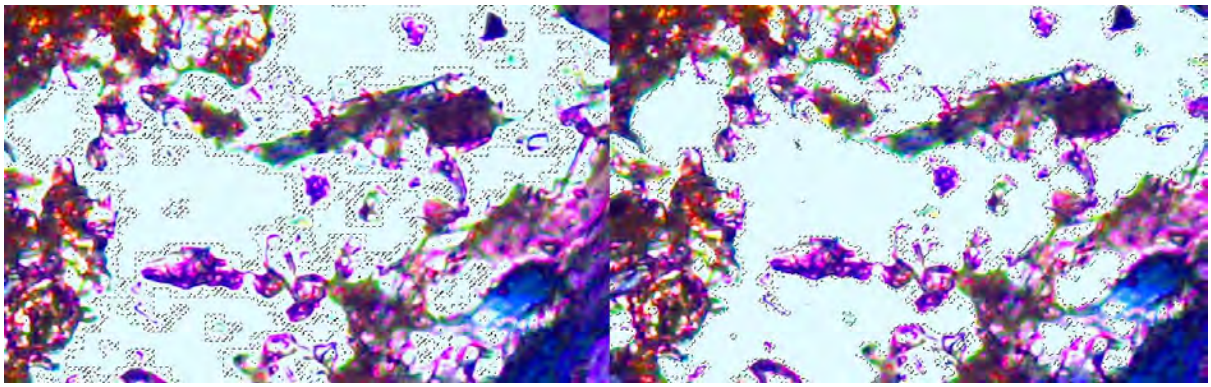

Figure 3: The dashed line shows the pixels that were colour-selected using white colour selection (left). To achieve a near pixel-perfect result (right), the "Expand Selection" tool is used. This does not introduce non-feldspar pixels (i.e. anything with clear colour) into the selection. Instead, white pixels with subtle hues bleeding over from surrounding minerals are included.

Thirdly, the high-saturation image was used to manually overpaint all titanites and epidotes that display an oversaturated orange, in clear contrast to the oversaturated blues of the amphiboles. Curiously, Adobe Photoshop struggle to differentiate these two colours when using the "colour-selection" tool. Alternatively, one can subtract the previous two layers from the total and remove all titanite pixels from a third, newly created layer. This would have the same effect as the thin sections, practically, contain only opaques, feldspars, glaucophane/titanite intergrowth and epidote (all pixels – colour selected opaques – colour selected feldspar – manually overpainted titanite and epidote = blue amphibole).

Finally, layers were subtracted from each other using the command “Ctrl+left”+ click on the layer icon, then press the delete key with the target layer selected. This step ensured there was no overlap between individual layers, preventing double-counting of pixels. Lastly, using the “histogram” function, the pixels of each overpainted layer were used to calculate mineral abundance.

To test the accuracy of this method, the same images were analysed twice by another student familiar with thin-section analysis. Uncertainty for feldspar and opaque is below 1%, whereas for titanite-epidote it is around 4%. The greater uncertainty for titanite-epidote is due to differing interpretations. As outlined in the petrographic observations section below, titanite and epidote exhibit extremely similar optical properties. They are therefore easily confused even under a microscope, which explains the differences in point counting.

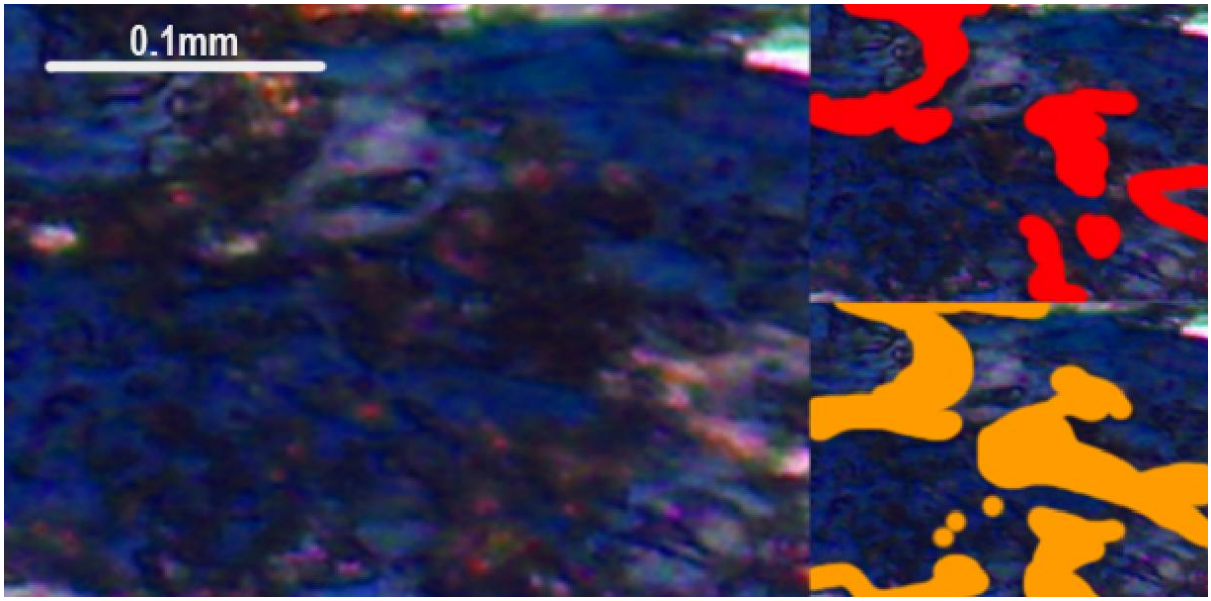

Figure 4: A glaucophane crystal that hosts a large number of inclusions (left). On the right, titanite was highlighted by two different students (red, orange). Differences in the interpretation of what should be marked as titanite and varying thresholds for “what should be counted” are responsible for the differences in the calculated results. Unarguably, these factors persist in traditional point-counting, too, when deciding which grain the point lines up with or which mineral that grain is.

3.3 Mineral chemistry

The lab manager at Uppsala University's microprobe lab carried out the investigation. The provided results were several hundred data points in thin section RE2439b and RE46. Here, major elements were measured in weight per cent (wt%). Beyond that, EDS images of individual crystals, such as REE-zoned epidote and titanite-ilmenite, were acquired.

Using the data gathered through the microprobe, the amphibole chemistry was recalculated using an Excel sheet produced by Locock (2014). In the input settings that define how the calculation is run, orthorhombic was set to false (as the amphiboles are not orthorhombic), as well as using the setting for initial "M3+/ΣM?" set to false. If set to true, "*the initial values for the valence states of Fe and Mn* [would] *be retained throughout the algorithm*" (Locock, 2014). This means that values for FeO and Fe_2O_3 would have to be provided. Since this was not the case, and both Fe^{2+} and Fe^{3+} values are required for later analyses, this setting was set to FALSE. The recalculated values were analysed and plotted using the ioGAS software (IMDEX, 2026, version 8.3).

3.4 Whole-rock geochemistry

Three samples, one plagiogranite and two greenschists (RE2439 and RE40, RE46), were cut and crushed in the PetroTectonic laboratory at Stockholm University. Sample RE2439 is a plagiogranite and displays three different domains, as described below. Therefore, the three domains were cut and crushed separately, and the major elements were determined for each. Rust stains were removed and appear to be most abundant in the greenschist sample RE40. The samples were crushed using a Retsch RS200 vibratory disc mill with tungsten grinding sets. Plagiogranite domain samples were ground at 900 revolutions per minute (RPM) for 90 seconds. Greenschist samples were ground at 750 RPM for 90 seconds. Here, a lower RPM was chosen based on the softness of the greenschist. Between samples or domains, the instrument was carefully cleaned with compressed air and ethanol to prevent cross-contamination.

In these samples, major elements were determined by inductively coupled plasma atomic emission spectrometry (ICP-AES; SARM-CRPG, Nancy). Bulk-rock glasses were fused at 980 °C by mixing appropriate proportions (1 %) of fine-grained rock powder with di-lithium tetraborate. Then, the glasses were dissolved in a mixture of HNO3 (5%), H2O2 (0.5%), and glycerol (10%) before analysis. Details of the method used in the analyses are provided by Carignan et al. (2001). Uncertainties at 1σ are 5% for the ICP-AES data. In addition, separate analyses of the Fe2+ content of the samples were performed at SARM-CRPG (Nancy, France) by titration with potassium dichromate after dissolution of the samples in an HF–H2SO4 mixture containing H_3BO_3 and H_3PO_4 (Manzotti et al., 2020).

The results were analysed and plotted using the ioGAS software (IMDEX, 2026, version 8.3).

3.5 Thermodynamic modelling

A pseudosection is a graphical representation of stable mineral assemblages in metamorphic rocks as a function of different variables, such as pressure-temperature (P-T), pressure-composition at fixed T (P-x) or other relevant properties. The former would be considered isochemical, meaning at a fixed bulk composition (Yakymchuk, 2017).

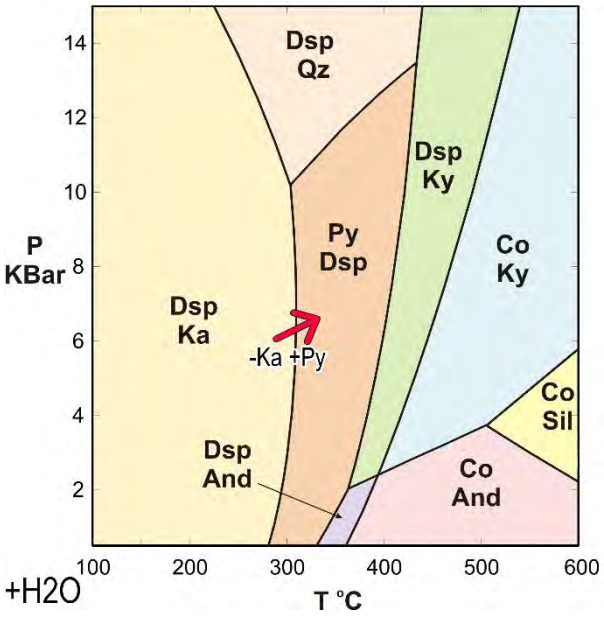

Figure 5: Simplified pseudosection modified after SERC (2007). Here, the red arrow indicates a possible prograde path across a univariant line. +H2O in the bottom left indicates that water is always present.

A pseudosection contains divariant fields and univariant lines. For example, the yellow field in the simplified pseudosection in Figure 5 indicates which minerals are stable under these conditions, in this case, Dsp and Ka. Within the field, both P and T can change without the mineral assemblage changing. If a rock were to follow the path indicated by the red arrow, it would cross a univariant line, entering a new stability field. Under the new conditions, Py and Dsp are stable. The univariant line can thus be called the Ka-out Py-in, or the -Ka +Py line. At the same time, the line represents the -Py and +Ka line if the rock were to cross it in the opposite direction. In many pseudosections, fluids are assumed to be present at all conditions. Since this would clutter the graphic, it is often indicated with a $+H_2O$ somewhere in the figure.

Thermodynamic calculations were performed using the Theriak-Domino Software version 2023.06.11 together with the internally consistent thermodynamic dataset ds6.2 by Holland and Powell (2011). The MnNCKFMASHTO system ($Na2O–CaO–FeO–MgO–Al_2O_3–SiO_2–H_2O–TiO_2–Fe_2O_3$ ± MnO ± K2O) was used, and fluids were assumed to be present. Results were calculated for 350-500 °C and 4-12 kbar based on the results of Koller (1985) and the Berlin group. Theriak-Domino does not produce ready-to-use pseudosections; the results must first be prepared. The software output, shown in Figure 6, produces the divariant fields and

univariant lines that define the chemistry. For this analysis, 428 univariant lines and corresponding equations were produced. It must be noted that equations produced by the software do not include geometry, i.e., the left side of the line does not necessarily equal the left side of the equation. Instead, this geometry must be constructed by the user. As an example, lines 103 and 104 define a field with a stable mineral assemblage. Therefore, one half of both equations must be equal, as highlighted in red in Figure 6.

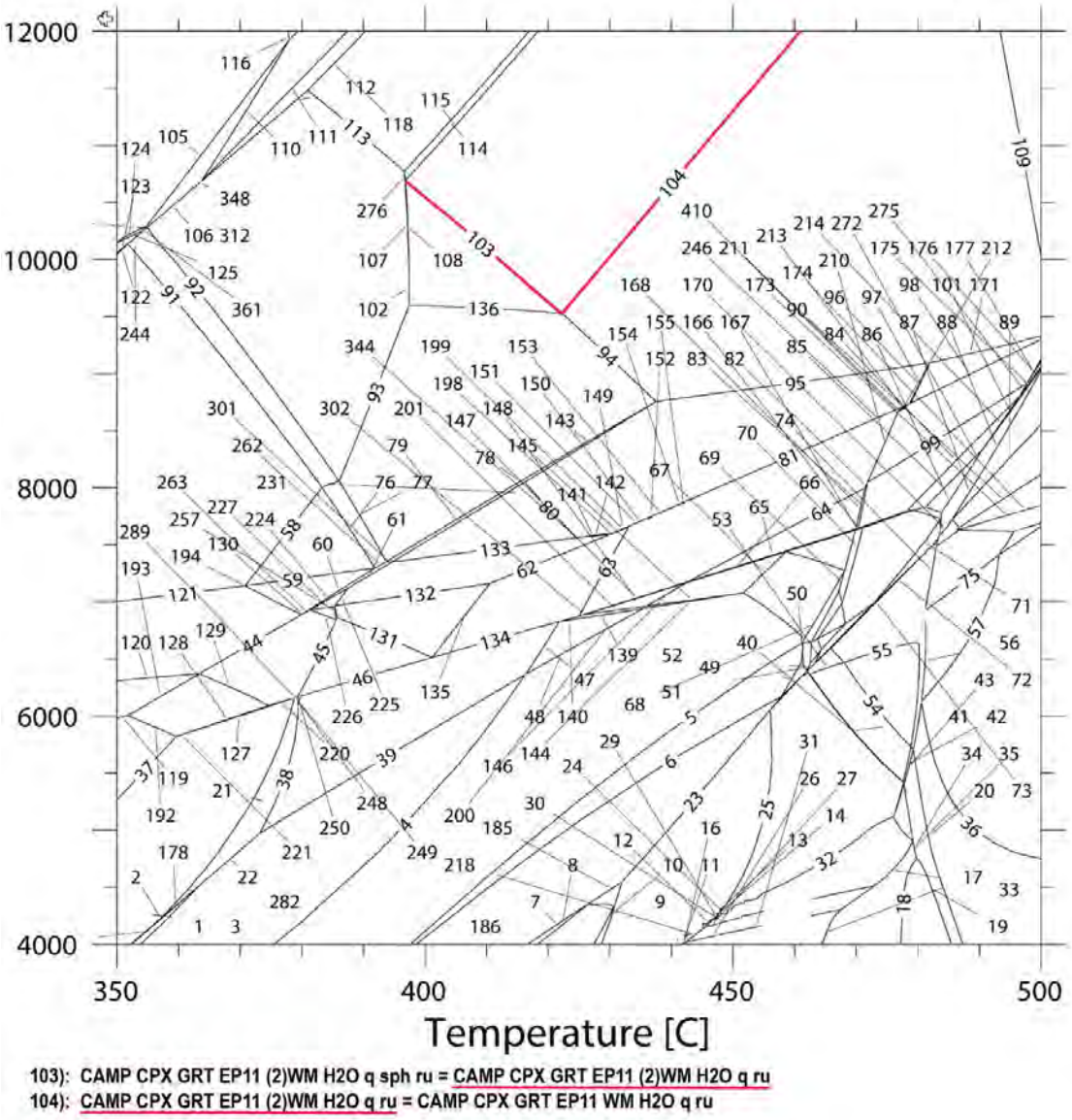

Figure 6: The unedited pseudosection. Often, several numbers appear to point to the same univariant line; in this case, tiny fields with different mineral stability are found between the two. Unfortunately, especially in areas with many small fields, it is not always clear which number points to which line. In these cases, field stability must be carefully constructed by going from neighbour to neighbour.

Subsequently, the common part of the two equations defines the stable mineral assemblage in the field. This process must be repeated for all relevant fields until the grid is constructed. It should be noted that minerals need not be observable if they are calculated to be stable in a certain field. This is due to their potential low modal amount, as will become apparent below.

4 Petrographic Investigation

4.1 Plagiogranite

Plagiogranite samples were collected close to Glashütten bei Schlaining. Five samples were collected from a loose block in the forest, and one from a road cut along an access road. The sample locations are marked on the map in Figure 7 below.

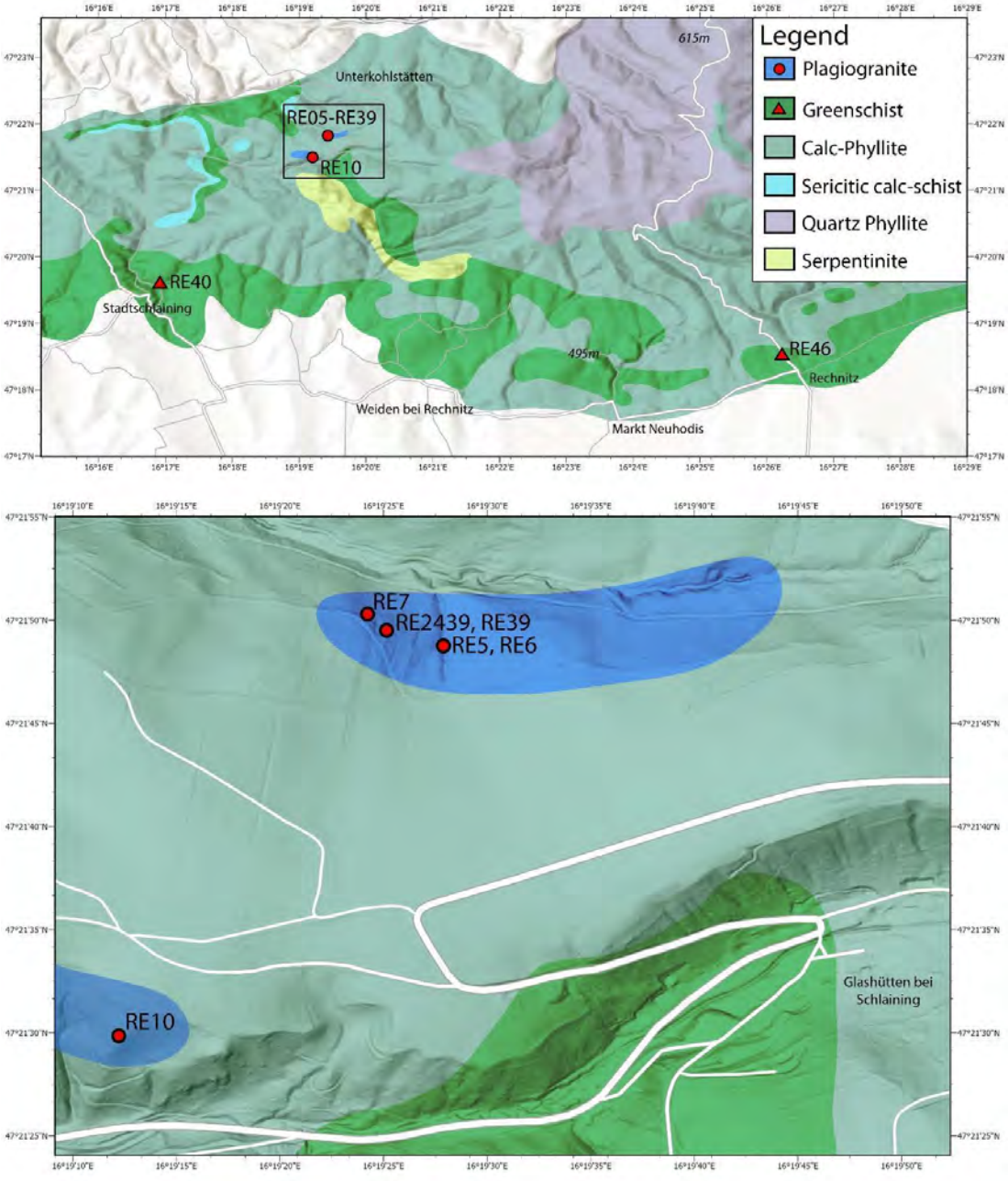

Figure 7: Map of the sample area. Bedrock information was extrapolated from the "Map of the Burgenland" from Schönlaub (2000). Based on field observations, the occurrence of blueschist in this area likely differs from that shown on the map.

Table 1: An overview of the samples. Fgln = ferro-glaucophane, rbk = riebeckite, ab = albite, ttn = titanite, ep = epidote, stp = stipnomelane, zrn = zircon, mag = magnetite, ilm = ilmenite, act = actinolite, chl = chlorite, ms = muscovite

Rock type	Sample name	Silicates	Non-silicates
Plagiogranite	RE39 / RE2439a / RE2439b	fgln-rbk, ab, ttn, ep, stp, zrn	mag, ilm
Plagiogranite	RE05	fgln-rbk, ab, ttn, ep, stp, zrn	mag
Plagiogranite	RE06	fgln-rbk, ab, ttn, ep, stp, zrn	mag
Plagiogranite	RE07	fgln-rbk, ab, ttn, ep, stp, zrn	mag
Plagiogranite	RE10 / RE10.2	fgln-rbk, ab, ttn, ep, stp, zrn	mag
Greenschist	RE46	act, alb, ep, chl, ms	—
Greenschist	RE40	act, alb, ep, chl, ms	—

4.2 Sample Description

In the hand sample, plagiogranites display uniform dark blue domains (hereafter referred to as Type 1) and greyish-white domains (hereafter referred to as Type 2) in alternating bands. Moreover, sample RE2439 contains a dark blue rafted block that, in the hand sample, hosts visible white albite grains (Type 3). The average mineral abundance for each domain (expressed in vol%) was estimated using Photoshop point counting, as described above.

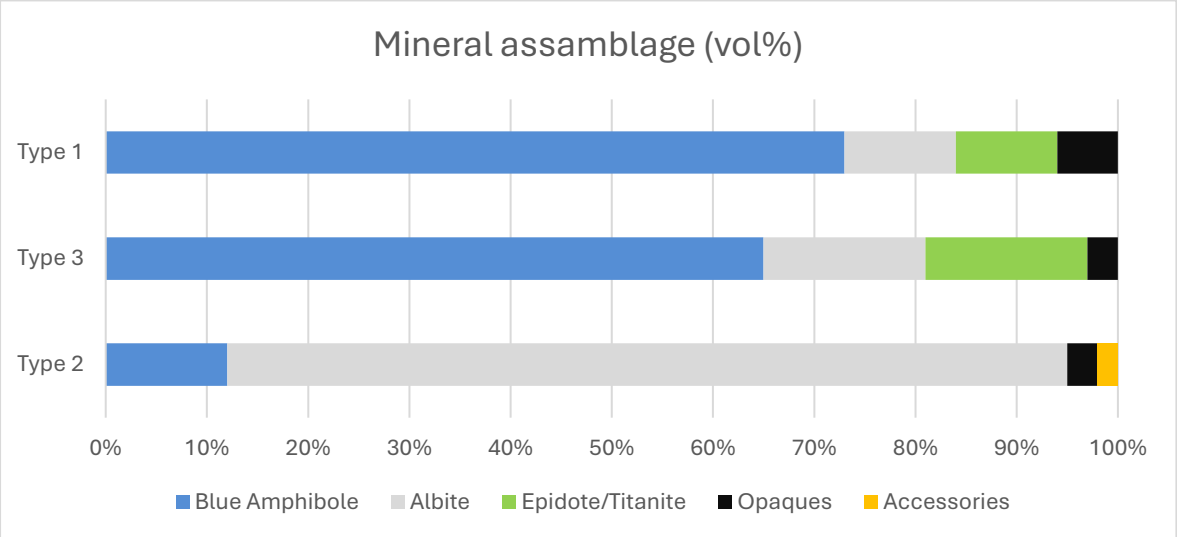

Figure 8: Average mineral abundance (vol%) for each domain. The distinct macroscopic features of Type 1 and Type 3 domains reflect a pronounced difference in the modal proportions of albite and blue amphibole. Epidote and titanite are grouped because they are very difficult to distinguish at the petrographic microscope due to their similar optical properties and often very small grain size. Accessory minerals that individually account for less than 2% are stilpnomelane and zircon (observed in Types 1, 2, and 3), and epidote (if observed in Type 2).

4.3 RE2439a and RE2439b

Two thin sections were cut from this rock, see Figure 9. In the following, they are described together unless otherwise specified.

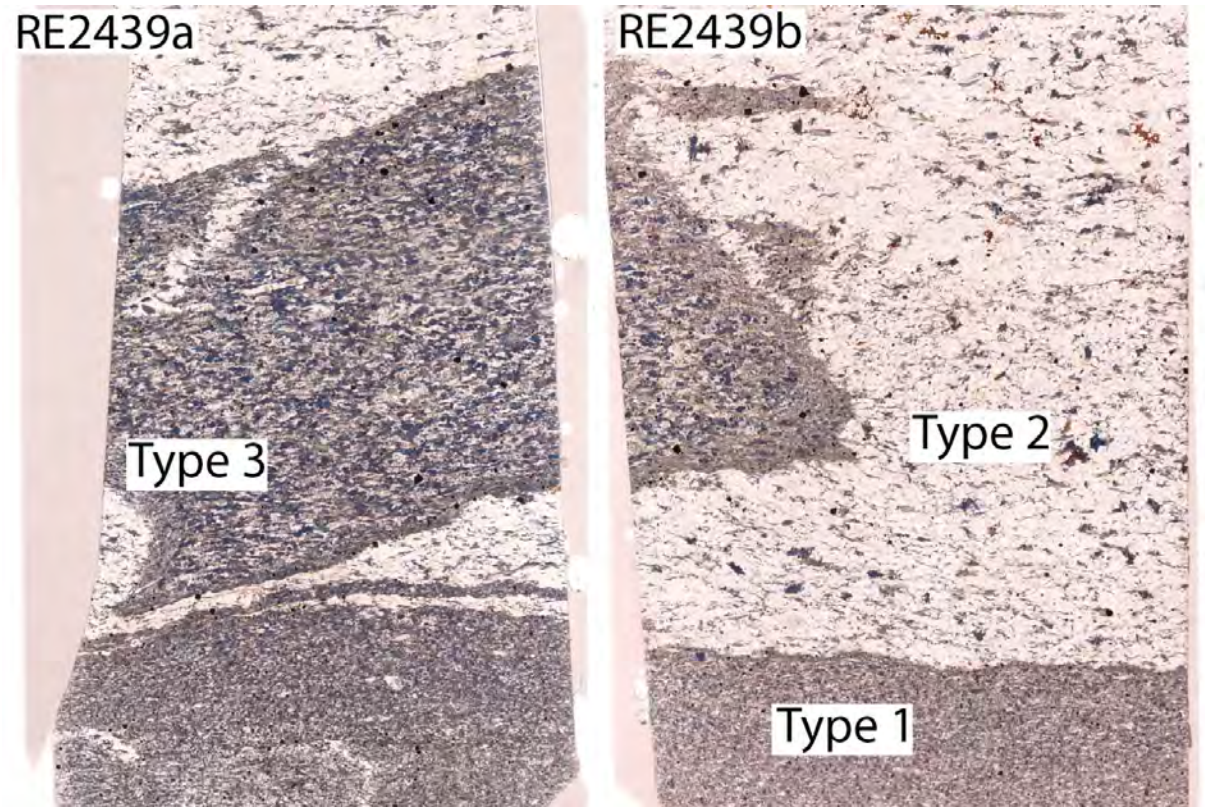

Figure 9: The image shows the two thin sections in their original fit. Even to the naked eye, the difference in the size of blue amphiboles is visible.

4.3.1 Type 1 domain

On average, the Type 1 domain contains blue amphibole (73%), albite (11%), epidote (10%), and magnetite (6%). It displays a finer grain size than Type 2 and Type 3 domains. In the Type 1 domain, a relic foliation (S1) is marked by amphiboles oriented at a high angle with respect to the main S2 foliation, which is defined by the shape preferred orientation of fine-grained (0.2 mm in size), prismatic, *blue amphibole*. A few *albite* veins cut the main foliation (Figure 9, bottom left). All blue amphiboles display deep blue pleochroism in PPL. Some crystals show deep blue cores with thin, slightly paler rims. In other crystals, this texture appears patchier (Figure 10a). A few large crystals display bluish-green zonation towards the rim, with sharp boundaries (Figure 10b). Most blue amphiboles contain *titanite* crystals.

Titanite inclusions are often elongated, almost always perfectly aligned with the host crystal's orientation, and vary in size from 10-100 µm (Figure 10c). While their colour in PPL is masked by the blue of the amphibole, their colours in XPL range from 3rd-order turquoise to pink, but appear slightly muted. Tight "cleavage-plane-like" morphology can be observed. Smaller, rounded inclusions of titanite, pale yellow in PPL, and 2nd order yellow to dirty brown in XPL, are concentrated in aggregates (Figure 10a).

A 0.4 mm-thick band rich in micrometre-sized titanites and *epidotes* separates the Type 1 domain from the neighbouring Type 2 domain (i.e. the albite-rich domain), which is described below. This feature is observed throughout the entire thin section of this sample.

Albite in this domain mostly occurs as small crystals (~ 0.1 mm in size). Larger crystals (up to 0.4 mm in size) are observed in the late veins that cut the main S2 foliation. Crystals in the matrix are generally pristine and uncracked, with rare large crystals exhibiting oxidised cracks. The majority of the crystals are untwinned, with only a few crystals displaying weak polysynthetic twinning. Randomly oriented inclusions of epidote, blue amphibole, green amphibole, and zircon are visible in the largest albite crystals. (Figure 10d and e)

Epidote (10f) is not only included in albite, but it also occurs as 0.1 mm long crystals in the matrix. Some crystals display a core-to-rim zoning, with 2nd-order interference colour ranging from purple in the cores to orange in the rims. Other crystals show 3rd-order interference colour (neon bluish-green). In the 0.4 mm-thick, titanite-rich band that separates Type 1 and Type 2 domains, individual, large, twinned epidote crystals are observed. It should be noted that epidote and titanite are remarkably similar in the samples investigated. The main differences are the more vibrant 3rd-order interference colours of large epidotes, twinned crystals, and clear core-to-rim zoning. Micrometre-sized aggregates or small, individual crystals can only be identified with confidence if the chemistry is known (i.e. at the microprobe).

Magnetite in this domain is common: it occurs as euhedral crystals (from 10 µm to 0.2 mm in size) and displays a grey-brownish colour in PPL reflected light and is isotropic in XPL reflected light. Almost all crystals are inclusion-free, as proven with the microprobe. However, due to the imperfect polishing, crystals contain holes and pits that reflect light as if they were inclusions.

Ilmenite occurs in minor amounts in this domain. It appears as shapeless, “worm-like” blobs with properties similar to magnetite under PPL, but is anisotropic under XPL.

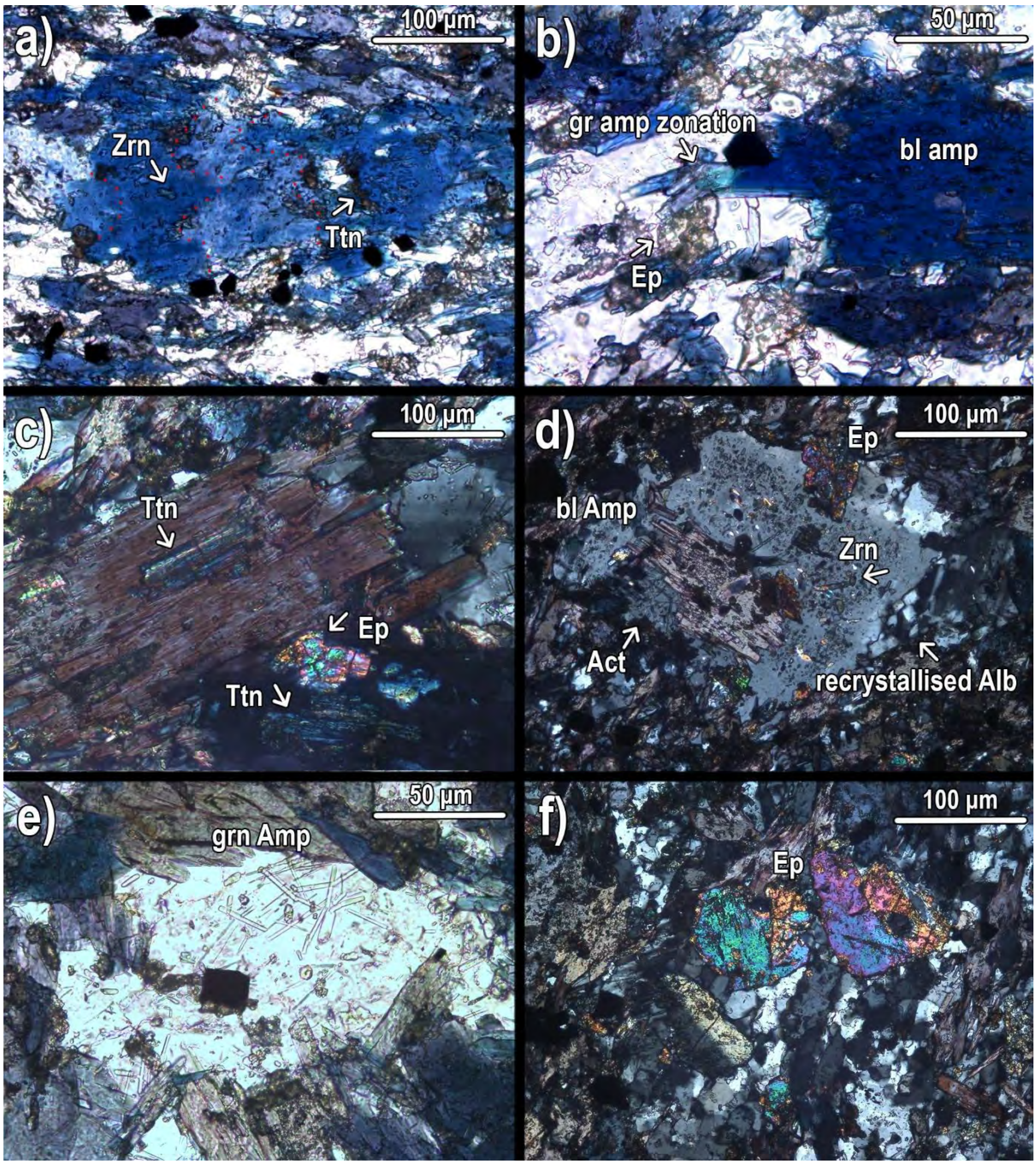

Figure 10: a) Blue amphibole showing a patchy zoning, a common feature in the Type 1 domain. Tiny zircon and titanite are included in blue amphibole (PPL). b) Blue amphibole displaying a green rim (PPL). c) A blue amphibole displaying inclusions of both titanite and epidote. Here, the difference between titanite and epidote is clearer through their relief and colour differences (XPL). d) An albite crystal displaying inclusions of blue amphibole, green amphibole, epidote, and zircon. Albite is partially dissolved and recrystallised at its edge (XPL). e) Randomly oriented actinolite inclusions in albite (PPL). f) Twinned epidotes in a fine-grained recrystallised albite (XPL).

4.3.2 Type 2 domain

The Type 2 domain consists largely of albite (83%), with minor blue amphibole (12%), magnetite (3%), and stilpnomelane (2%). A relic S_1 foliation is defined by large (up to 0.5 mm in size) blue *amphibole* crystals that are oriented at a high angle with respect to the S_2 foliation. The latter is a weak fabric characterised by the preferred orientation of thin, prismatic, deep-blue pleochroic amphiboles (0.3 mm long). Furthermore, amphiboles cut perpendicular to their c-axis, thus displaying their intersecting cleavage planes, are typical in this domain and have not previously been observed to this degree. Amphibole crystals are generally cleaner, and crystals hosting titanite inclusions are far less common (Figure 11a) than in the Type 1 domain. *Titanite*, in those crystals that contain inclusions, is equally hosted in the core and rim of amphiboles.

In this domain, *albite* crystals are significantly larger than in the other two domains (up to 1.2 mm). The large crystals are frequently re-crystallised in fine-grained aggregates. Large albite crystals commonly display polysynthetic twinning. Small crystals (up to 20 µm in size) and only one large crystal (0.2 mm in size) show cross-hatched twinning (Figure 11b). Albite cores show numerous tiny inclusions and appear dirty. In addition, they contain tiny epidote and greenish-blue amphibole inclusions. Some crystals display an oscillatory pattern, defined by inclusion-free and inclusion-rich rings (Figure 11c). Larger crystals show fractures with random orientations.

Stilpnomelane, characterised by brown colour in PPL, occurs as decussate-texture aggregates (Figure 11e and f), often partially replacing blue amphibole. The original amphibole shape is locally preserved (i.e. stilpnomelane pseudomorph after blue amphibole).

Epidote occurs both as inclusions (up to 30 µm in size) included in albite and amphiboles and as large twinned tabular crystals (up to 0.5 mm in size) in the matrix. In PPL, it is faintly pleochroic and displays interference colours ranging from orange to blue, purple and neon green.

Magnetite (Figure 12 e and f) is found as euhedral crystals, ranging in size from 0.1 mm to 10 µm and displays a grey-brownish colour under PPL and is isotropic under XPL. Though still described as euhedral to subhedral, many crystals are broken up, displaying jagged edges. They are generally smaller and fewer in this domain than in the other two domains.

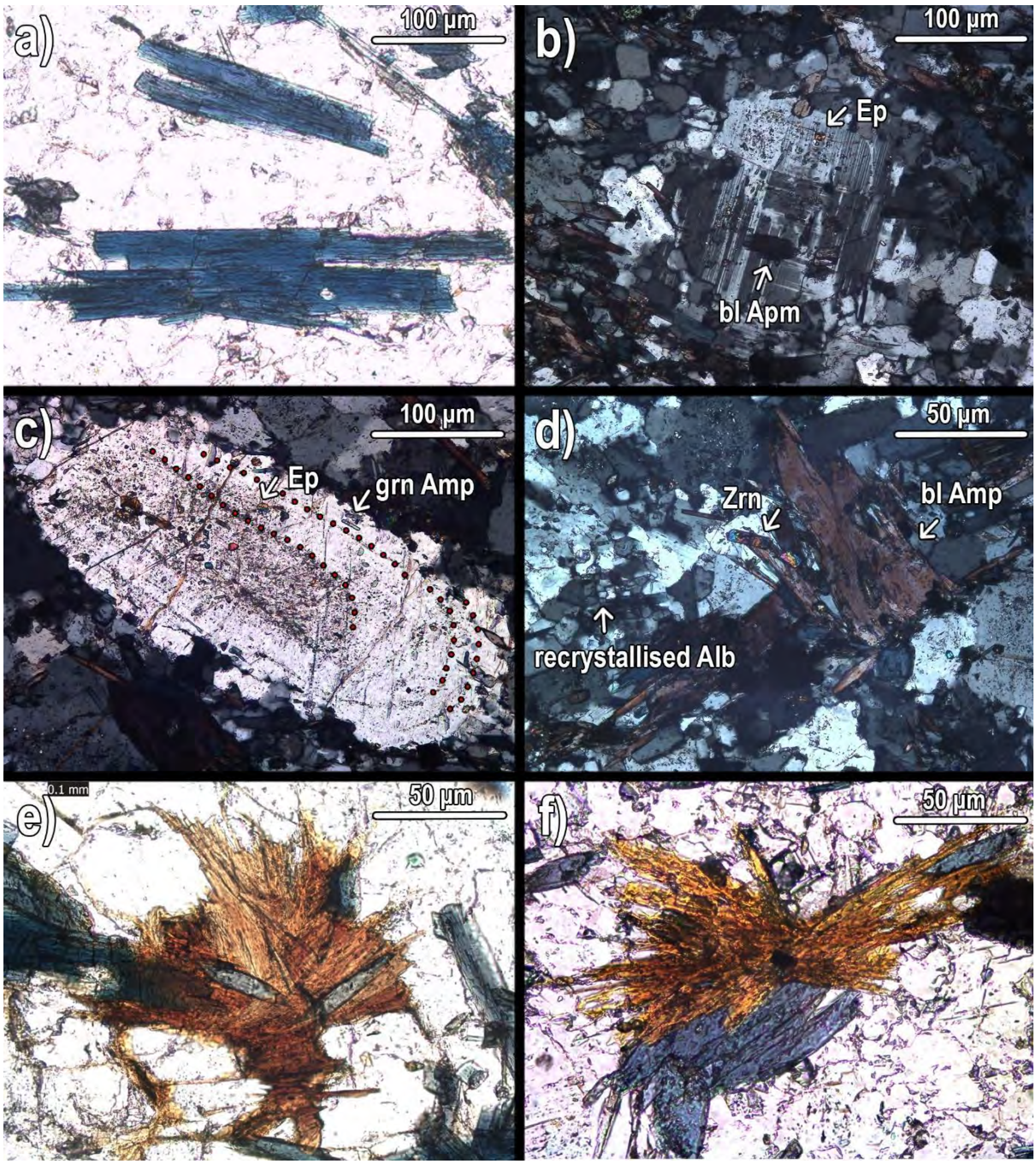

Figure 11: a) Two pristine, prismatic and inclusion-free blue amphibole crystals that are common in this domain (PPL). b) A large tartan-twinned albite with small epidote inclusions (PPL). c) Albite with an oscillary pattern of inclusion-free and inclusion-rich rings. They have been marked with red dots in parts of the crystal so as not to obstruct the view of the inclusions (XPL). d) Recrystallised albite with blue amphibole and a large, snapped zircon crystal (XPL). e) and f) Stipnomelane replacing blue amphibole, preserving the pseudomorph geometry (PPL).

4.3.3 Type 3 domain

In the hand sample, this domain appears as a rafted block that is 20° offset from the main foliation of the wall rock (Type 1). A remarkable difference to the Type 1 domain is its coarser grain size, with white patches visible to the naked eye. Indeed, this domain contains only (65%) blue amphibole, albite (16%), epidote (16%), and magnetite (3%), reinforcing the distinction between the two domains.

The S_2 foliation is defined by the shape-preferred orientation of blue *amphibole*, which is oriented at a high angle (rotated by about 20 °) relative to the wall rock (i.e., the Type 1 domain). The amphiboles are significantly larger (up to 0.6 mm long) than in the Type 1 domain, and their boundaries are slightly curved, giving them an oval-looking shape. As in the other domains, a relic S_1 foliation is marked by amphiboles oriented at a high angle with respect to the main S_2 foliation. In general, amphibole crystals in this domain display vibrant blue pleochroism and, in some crystals, pale blue, patchy zoning (Figure 12a, b).

Several large crystals host titanite inclusions. Their optical properties (high but pale interference colours, cleavage-like morphology, orientation relative to the host crystal) are identical to those of the titanite described in the Type 1 domain. Grainy, dark-brown titanite inclusions that resemble epidote are also common (Figure 12c) and were identified by microprobe analysis. In fact, reliable differentiation under the microscope is only possible if epidotes are either twinned, display unmuted 3rd-order interference colours, or show an epidote-titanite relief difference. Another striking difference in the Type 1 domain is the scarcity of inclusion-free amphiboles and the absence of green amphibole rims.

Albite in this domain is, on average, larger (up to 0.3 mm) than in the Type 1 domain and commonly shows polysynthetic twinning. Unlike albite in the Type 1 domain, they commonly contain numerous inclusions, such as greenish-blue amphibole needles, tiny green amphibole prisms (>10 µm), and high-interference epidote. While the smallest crystals are uncracked, larger specimens display randomly oriented, slightly oxidised cracks. Finally, a few veins cutting the Type 3 domain contain polysynthetically twinned albite crystals (up to 0.5 mm in size).

Epidote occurs as tiny, rounded grains (10 µm in size) forming aggregates or as elongated crystals (up to 0.3 mm in size) frequently associated with, or included in, albite. Epidote inclusions are often twinned, with pale blue to neon-green interference colours (Figure 12d). Smaller epidotes frequently display a core-to-rim zoning characterised by purple cores and orange rims. Several tabular, twinned crystals, each measuring 10 µm, occur in the matrix. These crystals, not observed in other domains, are always associated with plagioclase, either in veins or thin microlithons, see Figure 12d.

Magnetite is found as euhedral crystals, ranging in size from 10 µm to 0.2 mm, and displays a grey-brownish colour under PPL and is isotropic under XPL. Crystals of all sizes host numerous inclusions-like cracks that are easily confused with inclusions. *Ilmenite* occurs in one anhedral and blob-like shape. It looks remarkably similar to magnetite in PPL, but it is anisotropic.

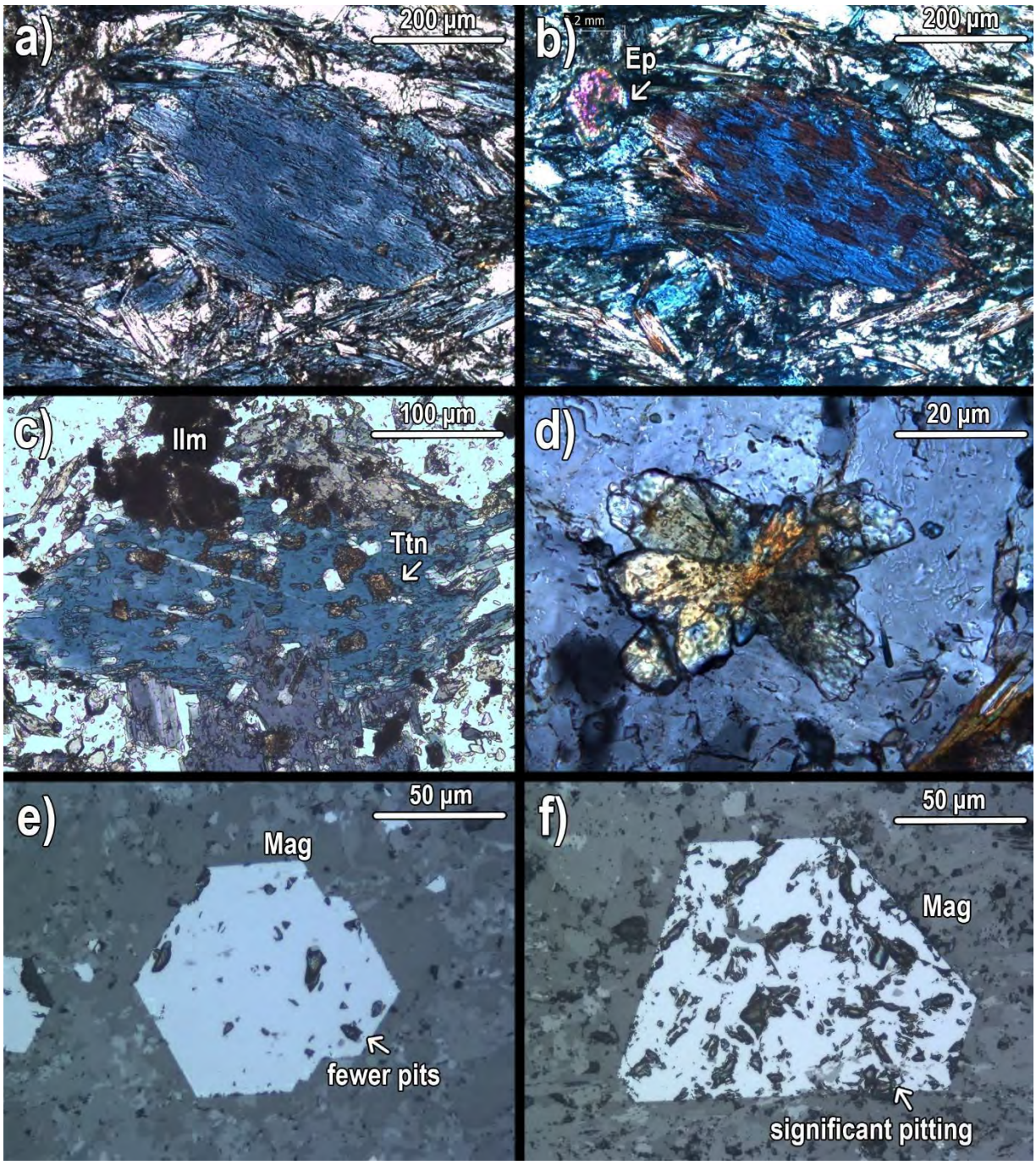

Figure 12: a) and b) Blue amphibole crystal in PPL on the left, and XPL on the right. Zoning in PPL is visible, but it becomes more striking in XPL. Small strings of inclusions are found in the core. c) A blue amphibole with dark brown, grainy titanite inclusions throughout the crystal (PPL). d) Tabular epidote crystals associated with albite. Pale twinning is visible. e) and f) Two typical magnetite crystals in reflected light. While e) contains fewer pits, f) is pitted significantly. Though they look like inclusions, the microprobe showed otherwise.

4.4 Greenschist

Two greenschist samples were collected, one north of Stadtschlaining and one in Rechnitz. In hand sample, they are pale green, rust-coated and can be broken by hand. Within the rocks, especially along cut faces, small rust-filled cavities are observed in the outermost 15% of the sample. Using a hand lens, these greenschists host interlayered pale green and grey domains. In sample RE40, the foliation is perfectly aligned with the long boundary of the thin section. In contrast, in sample RE46, possibly due to the way it was cut, the foliation is not parallel. Here, instead, the green (amphibole-epidote-rich) and grey (albite-rich) domains display wavy patterns, and white patches are visible in the hand sample. For each sample, one thin section was prepared.

4.4.1 RE46

This sample contains amphibole (54%), epidote (17%), albite (14%) and muscovite and chlorite at (7%) each, though their alteration texture makes clear identification difficult. The foliation in this sample is marked by the shape preferred orientation of prismatic amphiboles that were often cut perpendicular to their c-axis and by white mica.

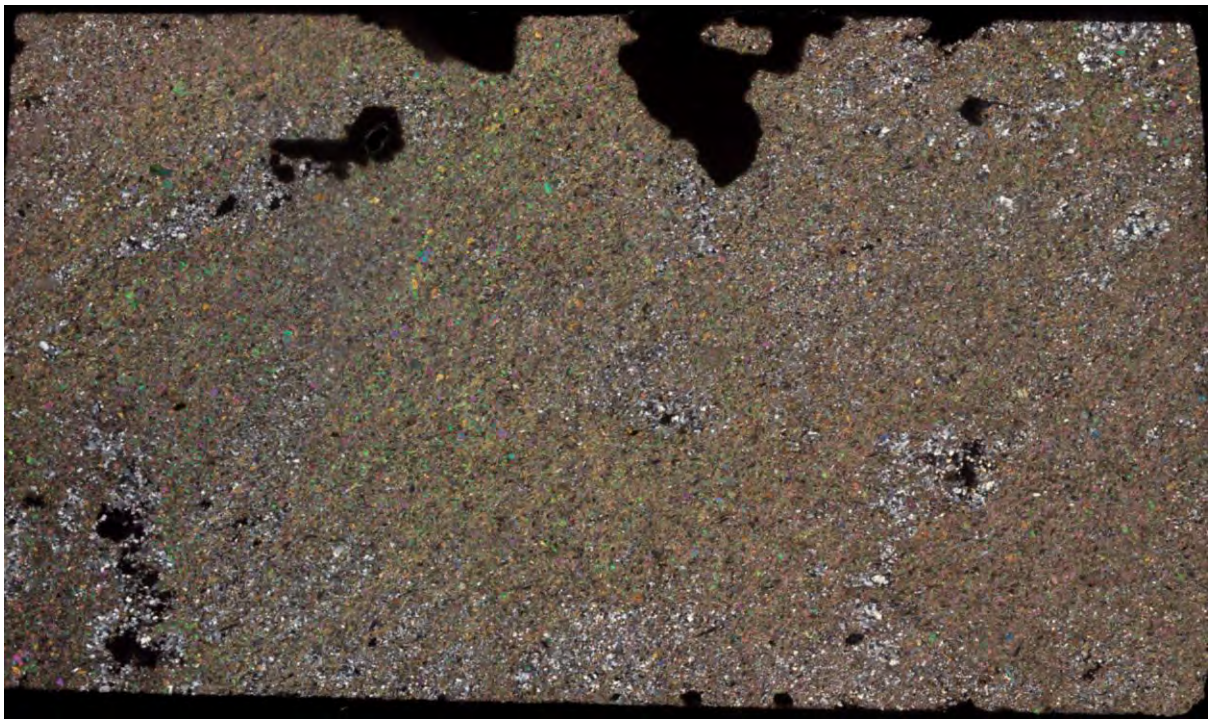

Figure 13: Thin section scan of sample RE46 (XPL).

In this sample, amphiboles appear to display two different sets of optical properties. *Amphibole I* (from 0.1 to 0.4 mm in size) are pale green and slightly pleochroic (Figure 14a) in PPL. Under XPL, smaller crystals, around 0.1 mm in size, show pale, brownish-yellow 1st-order interference colours. Larger crystals, up to 0.4 mm in size, display dark brown to vibrant orange cores with pale yellow rims (Figure 14b). Though most amphiboles are parallel to the foliation, some larger crystals, in or directly adjacent to albite-rich microlithons, are perpendicular to it. *Amphibole II* occurs as long blades (up to 0.8 mm in length) oriented parallel to the foliation. They show weak pleochroism and deep blue and brown interference colours in patchy zones with inclined extinction. These crystals can include epidote and feldspar, which are generally parallel to the crystal orientation (Figures 14c and 14d). Most amphiboles appear pristine regarding the very limited number of inclusions. Undeformed and uncracked amphiboles are dominant, but several crystals are partially obliterated. This manifests as bent crystal points, crystals with missing halves, or splayed ends.

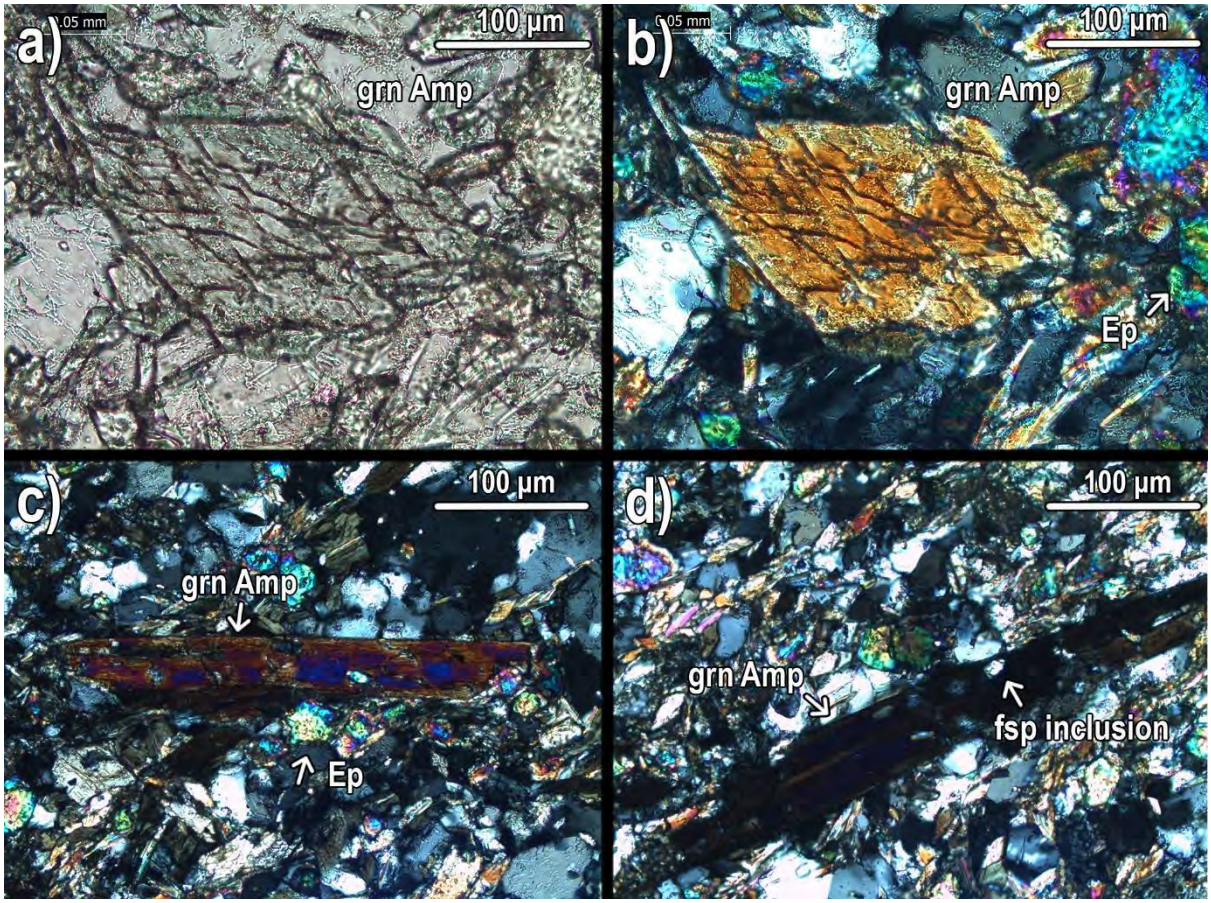

Figure 14: a) and b) Amphibole crystal in PPL with clear green (a) and XPL with vibrant brown (b). c) Amphibole and epidote crystals (XPL): the zoning of purple, blue and brown is clearly visible. d) Slightly rotated amphibole, showing inclined extinction and small albite inclusions.

Epidote in this sample is found as rounded to subrounded grains, rarely blocky, ranging from <10 µm to 0.5 mm in size. These crystals are strongly pleochroic and zoned. In PPL, the cores are neon green and the rims pink. In XPL, the cores display 3rd-order neon-green colour, and the rims are blue and purple. Both inclined and parallel extinction are observed. Some crystals show an opposite zoning (i.e. with 3rd-order neon-pink cores and neon-green rims)

Albite occurs in discontinuous bands alternating with amphibole-epidote domains. Crystals are small (< 0.2 mm) and commonly untwinned. Only simple twinning can be observed clearly, with single crystals suggesting polysynthetic twinning. Inclusions are generally limited to thin, green pleochroic amphibole needles (up to 50 µm in size) oriented parallel to the external foliation and tiny, rounded epidote grains (up to 10 µm).

Muscovite occurs in nearly continuous bands throughout the entire thin section. Under PPL, they are slightly green and pleochroic. As stated above, muscovite is often altered, blurring the lines between it and chlorite.

Chlorite is green and pleochroic under PPL and in XPL displays the typical anomalous interference colour (i.e., blue to pale brown). It is found in bands wrapping epidote and amphibole.

4.4.2 RE40

This sample, on average, contains 66% amphibole, 30% albite and 4% epidote. The main foliation in this sample is defined by discontinuous albite layers alternating with epidote-amphibole-chlorite domains. Within these domains, minerals frequently display a preferred orientation in shape, also marking the foliation. A few crystals are oriented at high angle with respect to the main foliation, suggesting the presence of an earlier relic foliation (S_1).

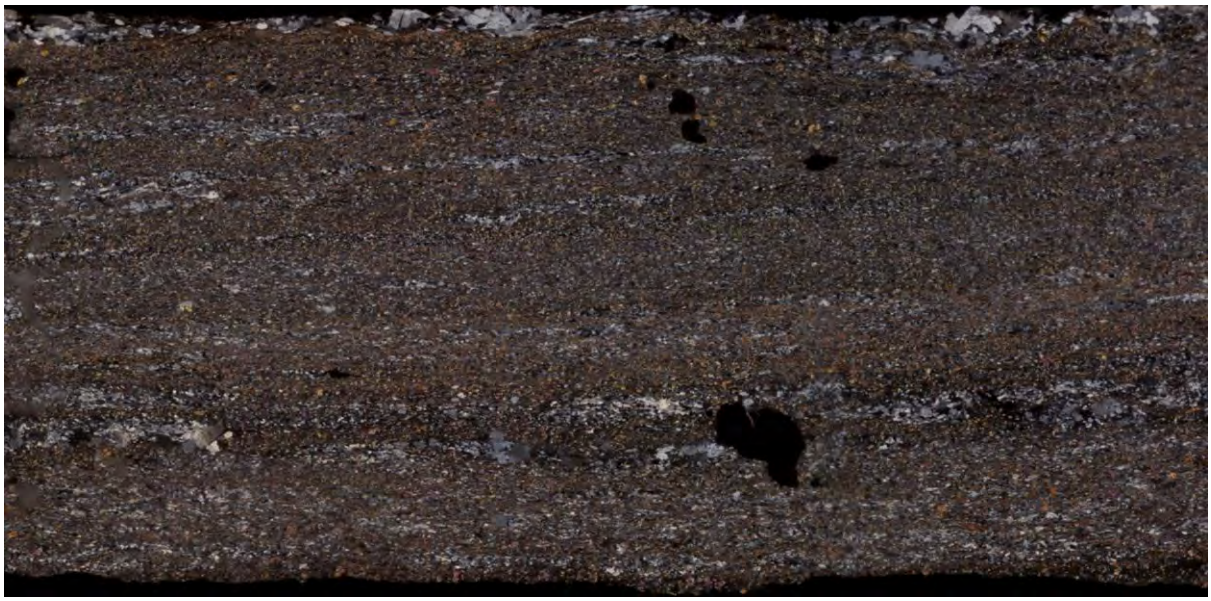

Figure 15: Thin section scan of sample RE40 (XPL)

Amphibole occurs as thin needles, up to 0.4 mm long, that are either perfectly straight when hosted in bundles in plagioclase or wavy, marking the foliation when hosted in an epidote-amphibole-rich microlithons. When hosted in plagioclase, they exhibit pale green pleochroism and 1st- to 2nd-order brown-to-purple interference colours. Under XPL, they display late 1st-order purple cores that transition to brown and, finally, to pale yellow at the rim. In the amphibole-epidote microlithons, they are significantly smaller and have an average size of 50 µm. Here, most crystals display brown cores in XPL, with only thicker crystals showing muted

blue cores and a general green tint in PPL. Larger crystals, reaching up to 0.3 mm in length, are blocky-prismatic, sometimes with splayed tips and display similar brown interference colours, but often with deep blue cores rimmed by purple (Figure 16a). While most crystals of this type are parallel to foliation,

There are two types of *epidote* in this sample. Both reach from 10 µm to 0.3 mm in size. One type of epidote shows no pleochroism and is pale yellow and blue in XPL, with rare, faint orange cores (Figure 16a, centre-right). The other kind displays neon-blue, purple, or green cores that transition to orange-brown inner rims with thin, pale-yellow outer rims. This type of epidote often displays zoned crystals, either diamond-shaped or ring-shaped (Figure 16b). Cleavage planes are often visible, and many of the larger blocky epidote crystals are cracked, obliterated and rotated. When rotated, pressure shadows are filled with chlorite.

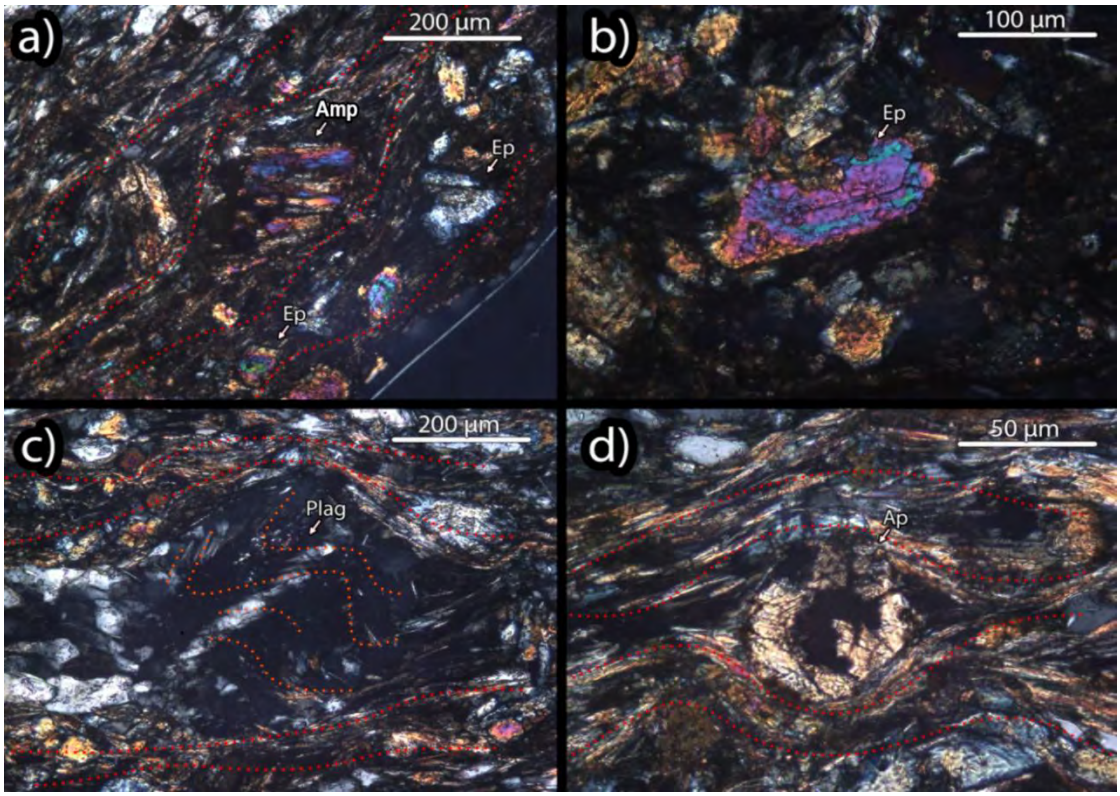

Figure 16: a) Clinoamphibole wrapped by the foliation (red dots). Two different types of epidote can be observed (XPL). b) Zoned epidote with purple core, blue outer core and purple rim (XPL). c) Albite with an internal foliation defined by thin amphibole needles (marked orange) and wrapped by the main S2 foliation (red) (XPL). d) An apatite crystal wrapped by the foliation (red).

Albite occurs in layers parallel to the main S_2 foliation. Some of these layers display rather large crystals (up to 0.6 mm in size) that are characterised by polysynthetic twinning, deformation twins, and undulose extinction. Some of these crystals are partially or totally replaced (i.e., recrystallised) by fine-grained albite aggregates. Other layers are entirely made of rather small crystals. Inclusions of thin dark green to brown amphibole needles oriented parallel to the main matrix foliation are locally observed. Their overall appearance is dirty, with numerous cracks propagating throughout larger crystals. These cracks are often filled with chlorite.
Apatite is hosted as a pre-tectonic accessory, recording rotation and a pressure shadow (Figure 16d).

5 Whole rock geochemistry

For this thesis, geochemical analyses were conducted on three rock samples: RE2439, a plagiogranite, and RE40 and RE46, both greenschists. As sample RE2439 has three macroscopically distinct domains, separate geochemical analyses were conducted for each domain (Types 1, 2, and 3). Then, to better understand the whole-rock geochemistry of RE2439, the average of these three domains was calculated.

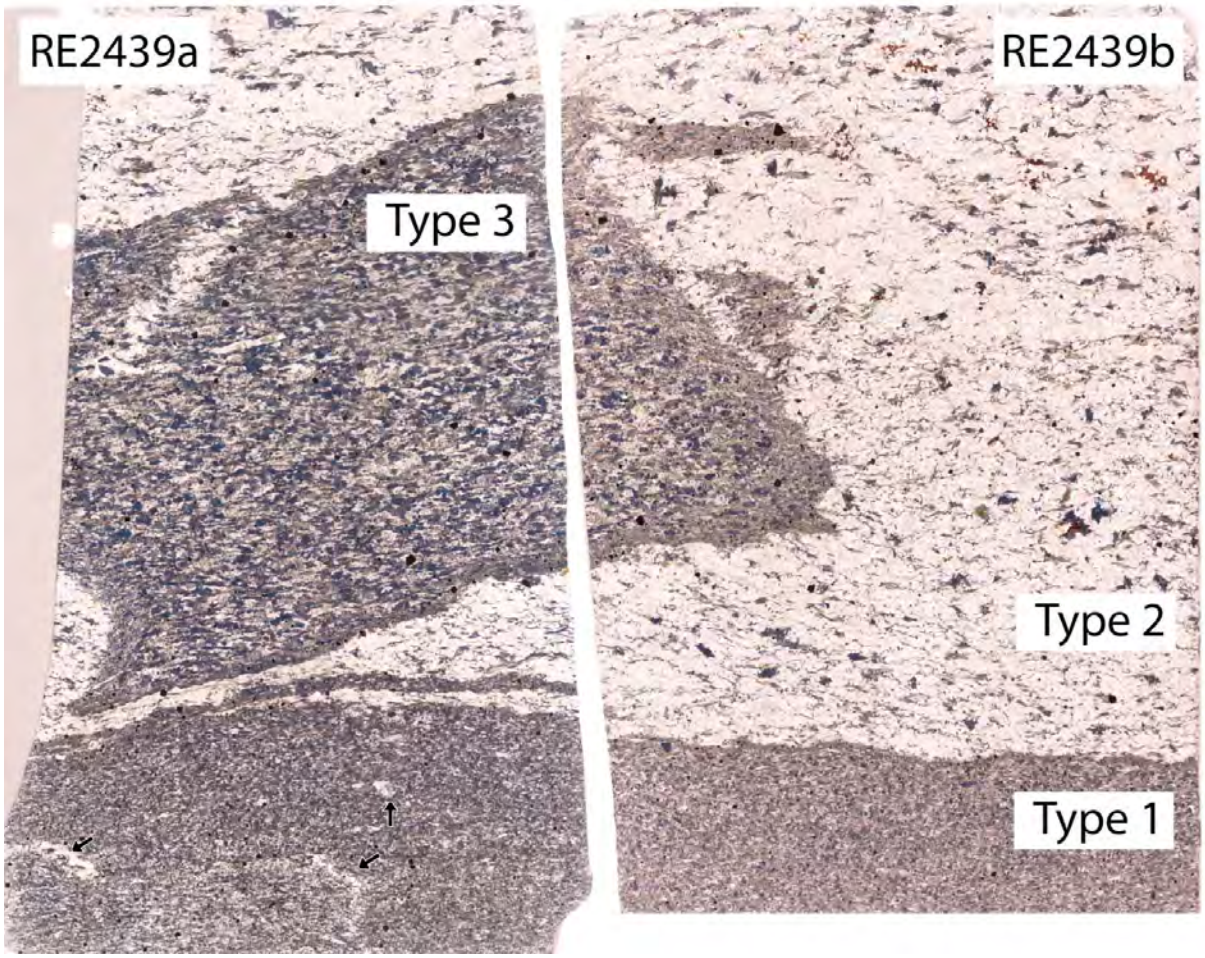

Figure 17: Overview of the type domains.

5.1 Plagiogranite

Sample RE2439, in its average composition, has an intermediate SiO_2 composition (56.82 wt%). It is rich in Na_2O (7.35 wt%) and high in total iron, expressed as Fe_2O_3 (15.47 wt%), Fe_2O_3 (7.09 wt%), and FeO (7.59 wt%). Al_2O_3 and MgO are low at (12.00 wt%) and (1.79 wt%), respectively. TiO_2, despite the abundance of titanite, is low at (1.6 wt%).

Looking at the domains individually, the Type 1 and Type 3 domains plot very close together, with their largest difference being Fe_2O_3, at (10.28 wt%) and (9.08 wt%), respectively. Moreover, the macroscopically observed differences (i.e., the white spots in the Type 3 domain) are confirmed by chemical analysis, which shows that the Type 3 domain has a 1.09 wt% higher SiO_2 content (54.08 wt%), 0.4 wt% higher Na_2O (6.57 wt%) and 0.26 wt% higher Al_2O_3 (9.98 wt%) than the Type 1 domain, facilitating the growth of plagioclase. Type 2 domain values differ significantly from the other two domains. This domain is richer in SiO_2 (63.41 wt%) and Na_2O (9.32 wt%), and lower in Fe_2O_3 (3.41 wt%) and FeO (2.91 wt%). All three domains display next to no K_2O (average 0.03 wt%) and no P_2O_5. These values are shown in Figure 18.

To place this data in a broader context, they are compared with geochemical data from the Rechnitz Window reported by Koller (1985), who, unfortunately, does not specify the methodology. In the diagrams below, Koller's data are plotted as hollow symbols, revealing several trends. Both Na_2O and Al_2O_3 correlate positively with SiO_2. By contrast, MgO, CaO, Fe_2O_3, FeO, and TiO_2 correlate negatively with SiO_2. In general, the chemical data compiled for this thesis agree well with those reported by Koller (1985). One major difference is the Mg#, which, in the samples analysed in this thesis, is significantly lower at 0.31 than Koller's value (i.e. 0.42). This difference is reflected in the slightly lower MgO in the Type 1 and Type 3 domains, which plot noticeably below the regression line.

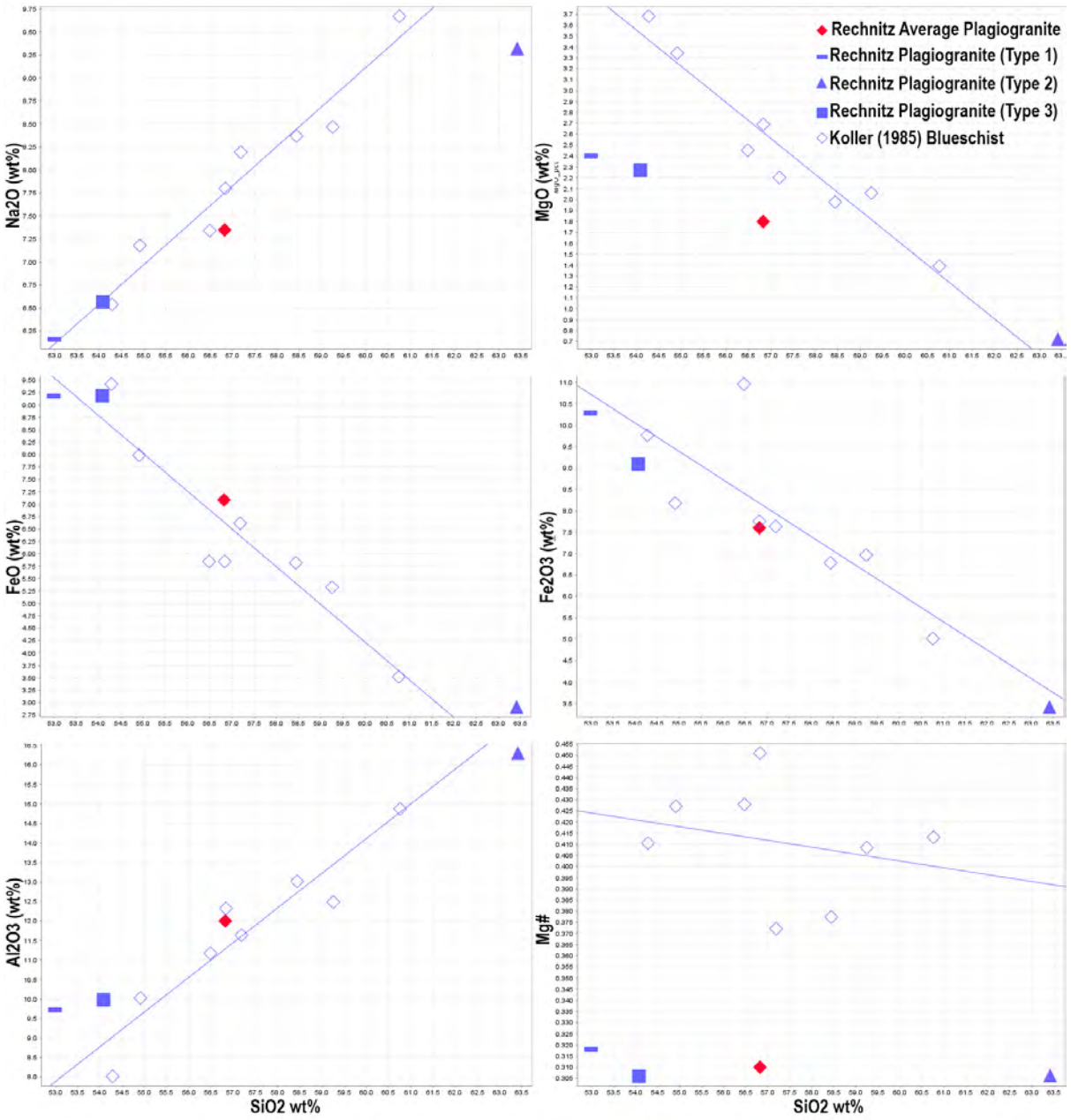

Figure 18: A selection of plots with relevant correlations shown as simple linear regression. Here, only the average composition should be compared with Koller's values, as he did not specify whether he separated the macroscopically distinct domains. Moreover, Koller's (1985) samples are labelled as blueschist. Initially, he classifies the relevant samples as blueschist based on macroscopic observations. Later in the text, he sub-categorises them as plagiogranites based on their composition.

5.2 Greenschist

Samples RE40 and RE46 display moderate SiO_2 contents (46.56-47.43 wt%) and similar LOI (3.43–3.81 wt%). Calcium in both samples is relatively high (9.2 wt%); by contrast, Na_2O is relatively low (2.42 – 3.62 wt%). There is a significant difference in K_2O between RE40 (<0.1 wt%) and RE46 (1.69 wt%). By contrast, total iron expressed as Fe_2O_3 is similar in both samples at (10.14 wt%) and (10.69 wt%), respectively. Here, sample RE40 displays lower Fe_2O_3 (2.53 wt%) than sample RE46 (5.32 wt%), but higher FeO (6.84 wt%) than sample RE46 (4.83 wt%). Moreover, sample RE46 shows lower MgO (6.25 wt%) than sample RE40 (8.73 wt%). As a result, the Mg# is identical at 0.69 for both samples.

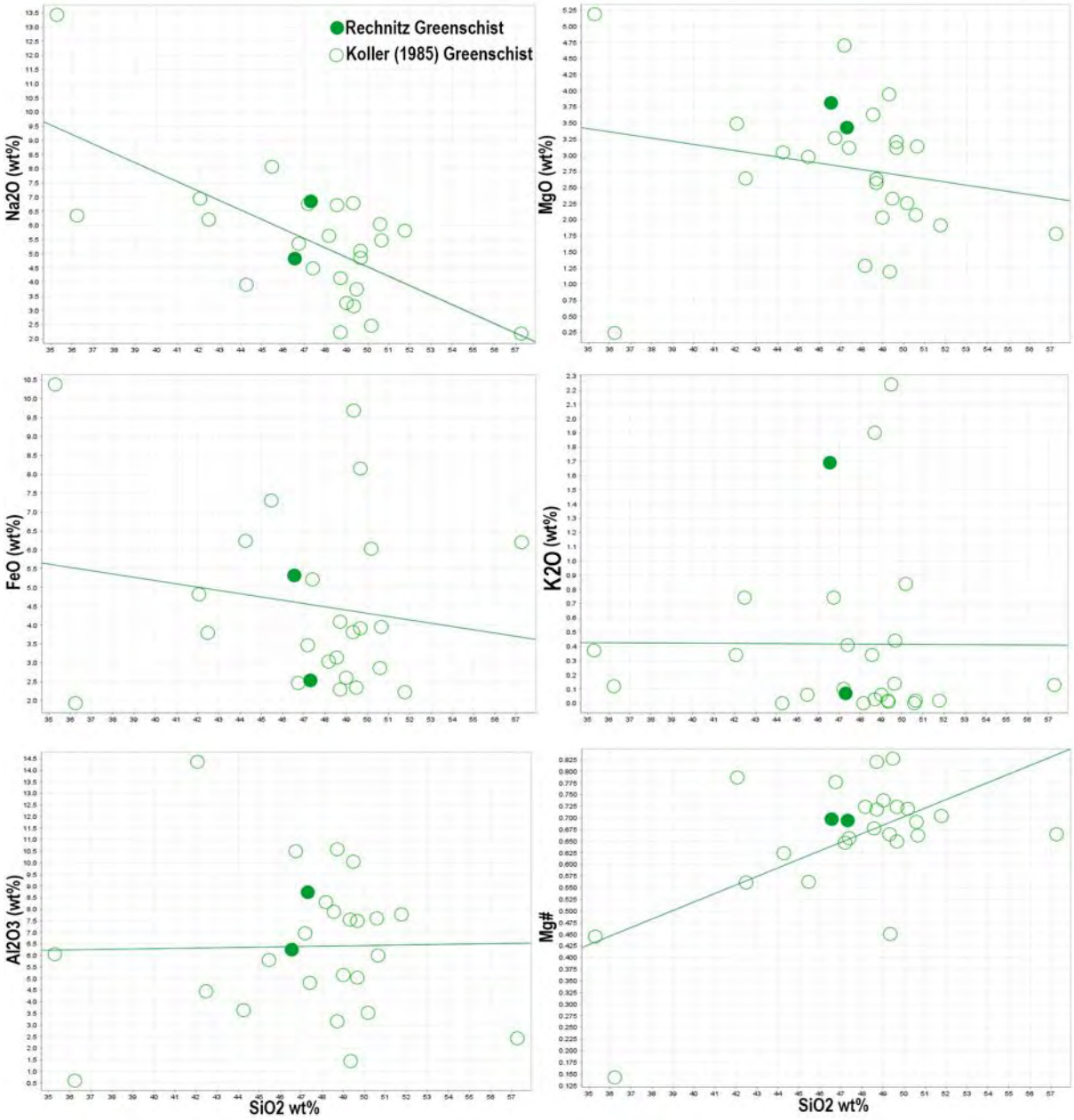

Figure 19: A selection of plots with relevant correlations shown as simple linear regression for greenschist samples.

Plotting these samples together with those of Koller (1985) makes the larger spread in the data points clearer, and the trends are more subtle. Most convincing are the negative correlations among SiO_2, LOI, and FeO, and the positive correlation between SiO_2 and Al_2O_3. Plots showing this are seen in Figure 19 above.

5.3 Protolith

In Figure 20, data are plotted in the diagram TiO_2 versus the mafic index, $M1=FeO_{tot}/(FeO_{tot}+MgO)$, which allows for the distinction between high-Ti and low-Ti ophiolites (Serri, 1981). In this diagram, the dotted grey line represents an empirical boundary between the two ophiolite types M1:Ti (0.35:0.15 wt%) to (0.75:2 wt%). All greenschist samples, and half of Koller's (1985) blueschist samples, plot firmly in the high-Ti ophiolite field. By contrast, sample RE2439 from this thesis, including its domains, plots in the low-Ti ophiolite field together with some of Koller's blueschists.

Expanding the scope of the analyses and considering other rock types from Koller (1985), a clear fractionation trend, as shown in Figure 20 below, is evident when TiO2 is plotted against M1, as proposed by Serri (1980). Firstly, the trendline shows a shallow increase in TiO_2 (from 0.25 to 1.5–2 wt%) up to an M1 of around 0.50, followed by a rapid increase in TiO_2 to above 7 wt% at an M1 of around 0.65, an environment in which TiO_2 is reported to slowly reach saturation (Serri, 1981). As shown in Figure 20, the fractionation trend of the plagiogranites and blueschists does not align with that of the other rock types.

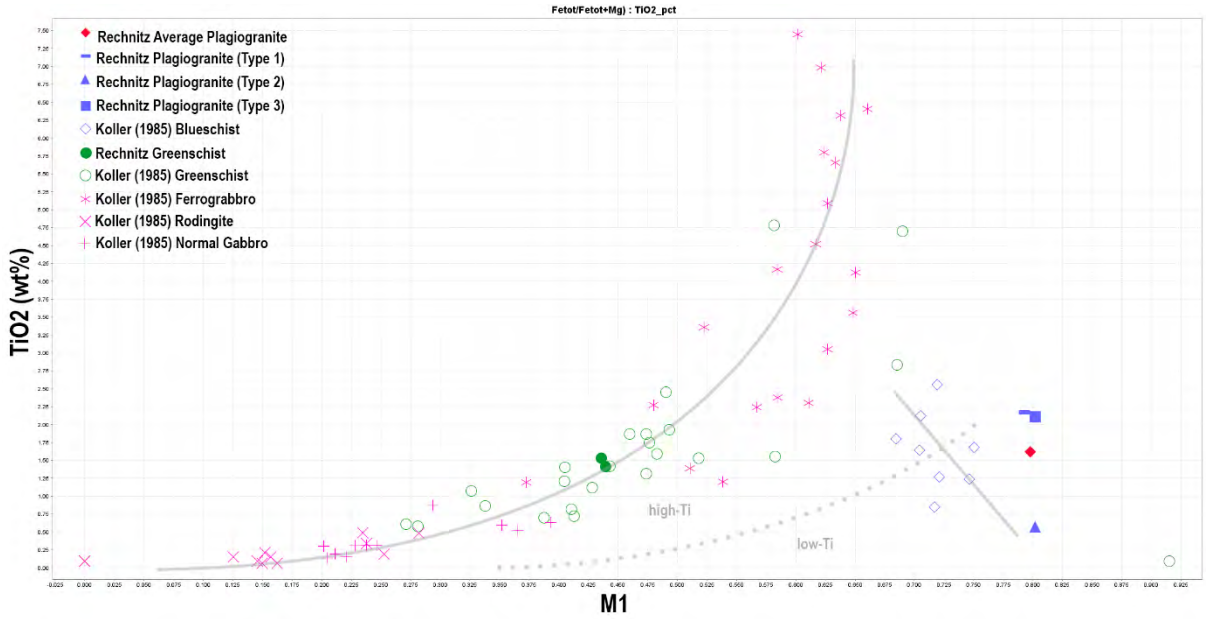

Figure 20: The figure shows the high-Ti/low-Ti boundary (dotted line), extrapolated from a hand-drawn figure in Serri (1981), along with the reported values. The two solid grey lines represent the fractionation trends extrapolated from Koller (1985). It should be noted that Koller does not provide a clear definition for "Normal Gabbros". The definition of Ferrogabbro is limited to "such rocks that are Fe and Ti-rich, with a gabbro-like texture".

In Figure 21, data are plotted in the ternary diagram SiO_2 – (Al_2O_3 + Na_2O + K_2O) – (TiO_2 + FeO_{tot} + MgO + CaO), together with data from Koller (1985) and Ohnestetter et al. (1981), the latter investigated acid rocks (plagiogranite).

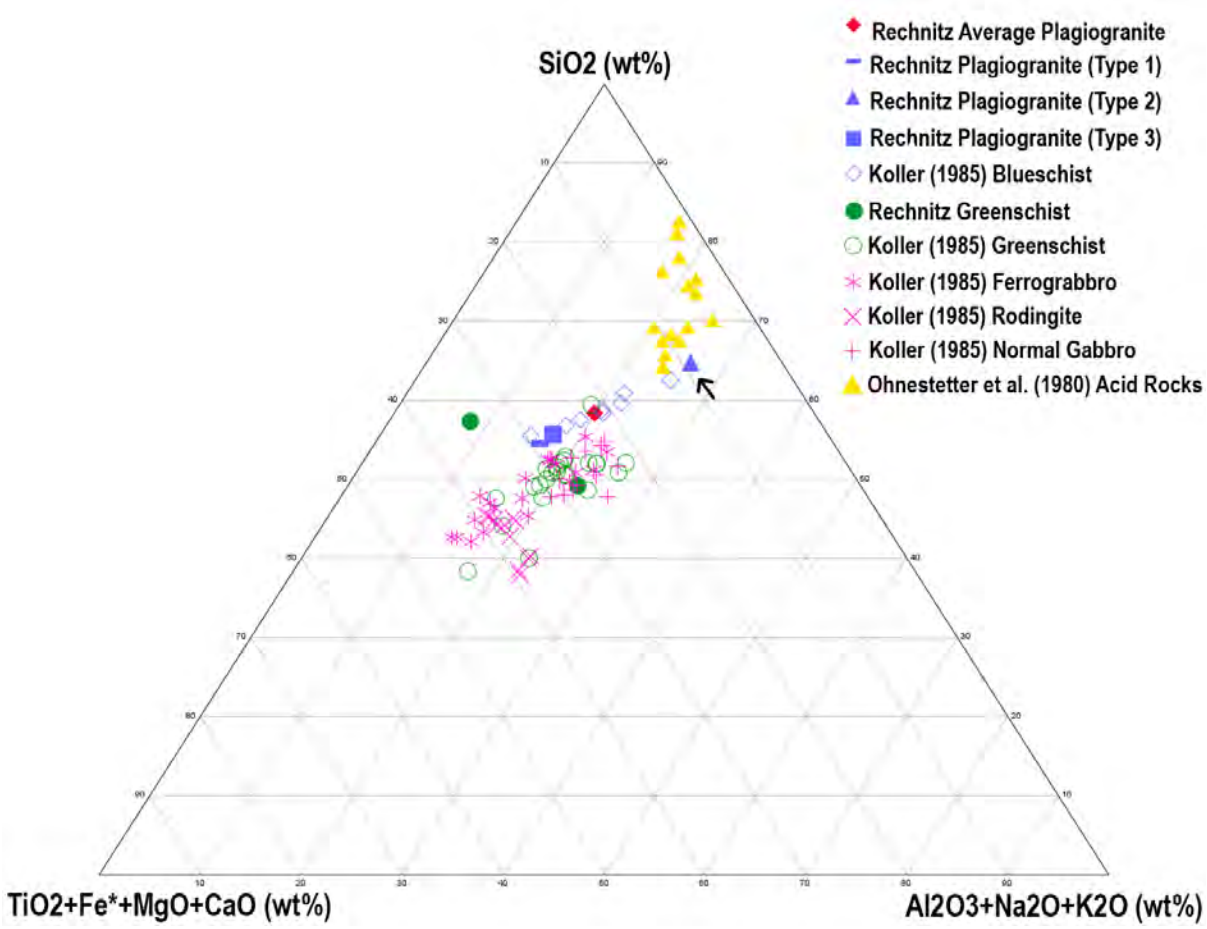

Figure 21: Ternary diagram plotting data from this thesis and Koller (1985) together with Ohnestetter et al. (1981). This shows good agreement between the Rechnitz Type 2 domain and the "acid rocks", i.e. plagiogranites from Ohnestetter (1981).

6 Mineral Chemistry

6.1 Amphiboles (plagiogranite, sample RE2439)

In the plagiogranite RE2439, amphibole was analysed in six crystals, yielding 40 individual data points across the core and rim. Chemical analyses are plotted in a diagram $Fe^{3+}/(Fe^{3+} + Al^{3+})^{VI}$ vs. $Fe^{2+}/(Fe^{2+} + Mg)^{VI}$, with ^{VI} indicating the C-site in the amphibole formula, which ideally contains 5 atoms per formula unit (a.p.f.u.). Amphibole data marking the S_1 and S_2 foliations, as well as core and rim, were plotted in Figure 22. Amphibole marking the S_1 foliation is Fe-glaucophane (16 analyses) and riebeckite (10 analyses). While their $Fe^{2+}/(Fe^{2+} + Mg)^{VI}$ ratio is relatively constant (0.67 – 0.76), their $Fe^{3+}/(Fe^{3+} + Al^{3+})^{VI}$ shows large variation (0.21 and 0.75). This chemical variation does not reflect a direct core-to-rim zoning: cores and rims are both Fe-glaucophane and riebeckite. Even within single crystals, there are large chemical differences, which are indicated with an arrow in Figure 22, highlighting two "endmember" compositions of a single crystal.

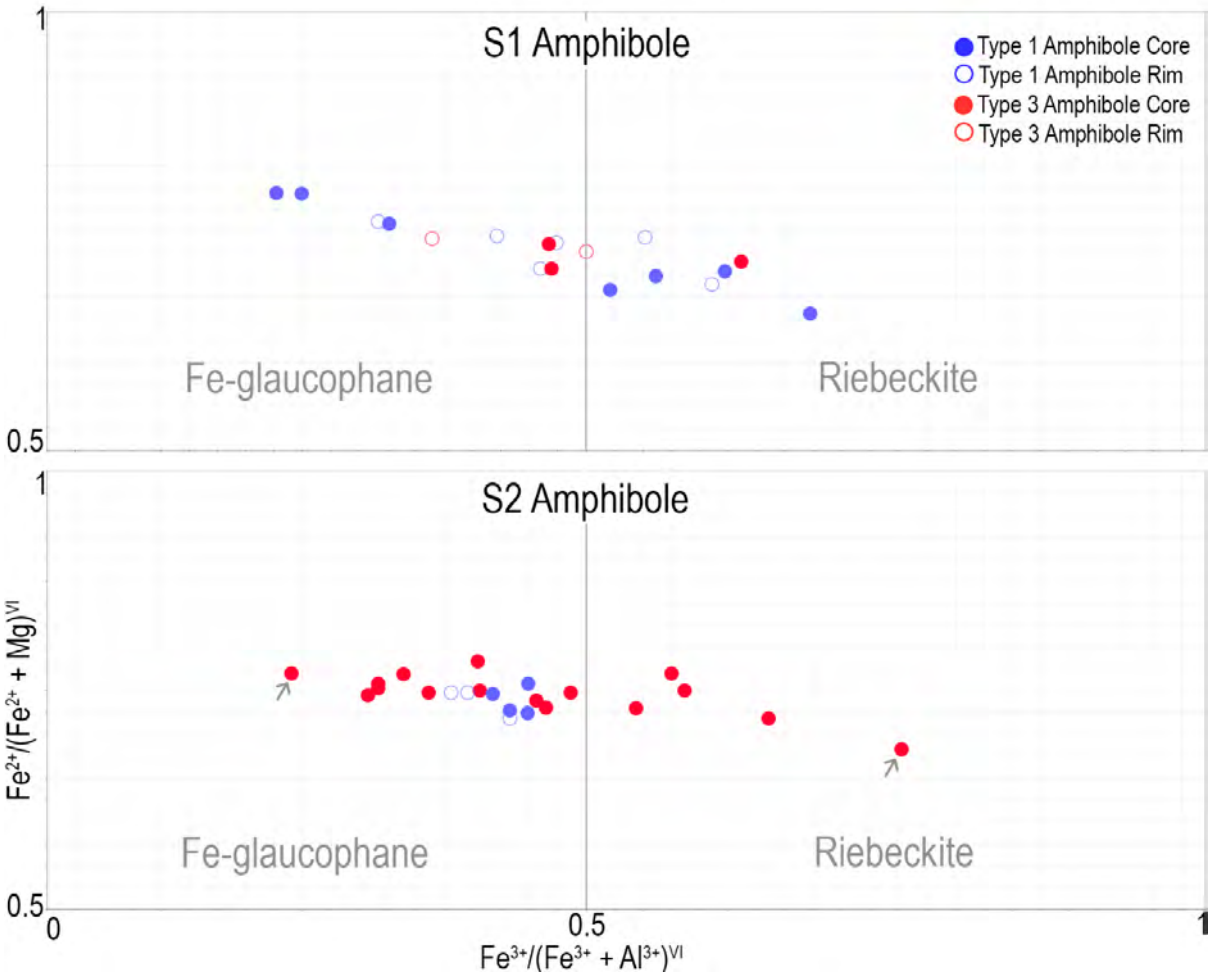

Figure 22: Composition diagram for Na-amphibole plotted in the $Fe^{3+}/Fe^{3+}+Al^{VI}$ vs $Fe2+/(Mg+Fe^{2+})$ separated by domain, core vs rim and S1 vs S2 foliation.

Both S1 and S2 amphiboles show strong chemical variation on average. By contrast, Type 1 domain amphiboles in the S2 foliation are chemically heterogeneous, with only a minor $Fe^{3+}/(Fe^{3+} + Al^{3+})^{VI}$ difference of 0.07 between core and rim of the crystal. Generally, intra-crystal chemical variation appears larger in Type 3 domain amphiboles than in Type 1 domain amphiboles.

6.2 Amphibole (greenschist, sample RE46)

In the greenschist RE46, a total of 27 chemical analyses of amphibole were performed. Data are plotted in a diagram with Si (a.p.f.u.) and $Fe^{2+}/(Fe^{2+} + Mg)^{VI}$ on the axes, respectively. All measurements exhibit very similar chemical compositions: Si ranges between 7.76 and 8 a.p.f.u. whereas the $Fe^{2+}/(Fe^{2+} + Mg)^{VI}$ ratio is between 0.7 and 0.76. All amphiboles fall in the actinolite field. Despite exhibiting more diverse optical properties (e.g., size, colour) as described in the petrographic observations section, the chemical composition of the analysed amphibole is quite homogenous and indicates a single amphibole type in this sample instead (i.e. actinolite).

Figure 23: All amphiboles measured in this sample show homogeneous chemical composition, plotting very close together. The largest chemical difference is 0.17 Si a.p.f.u.

6.3 Other Minerals

Albite is chemically homogeneous, rich in Al_2O_3 (19.15–19.95 wt%) and Na_2O (10.30–11.10 wt%), with negligible CaO and K_2O.

Epidote shows typical SiO_2 (37.49 wt%) and CaO (22.29 wt%), moderate Al_2O_3 (21.25–22.53 wt%) and FeO (12.52–14.68 wt%). The zoning observed under the microscope was confirmed by EDS, which displayed an REE-rich core and a depleted rim.

Table 2: A selection of representative chemical analyses of other minerals from the two samples

	RE2439						RE46	
Oxide (wt%)	Albite	Albite	Epidote	Epidote	Stipnomelane	Magnetite	Muscovite	Chlorite
SiO2	68.51	68.48	37.99	37.49	45.17	0.17	55.29	28.09
TiO2	0.00	0.01	0.01	0.06	0.08	0.03	0.14	0.06
Al2O3	19.15	19.95	22.53	21.25	5.91	0.00	24.97	19.54
FeO	0.15	0.22	12.52	14.68	26.53	94.51	4.45	20.27
MgO	0.01	0.00	0.00	0.00	5.93	0.03	4.46	19.68
MnO	0.01	0.01	0.14	0.59	2.12	0.21	0.04	0.33
CaO	0.02	0.82	23.33	22.29	0.16	0.00	0.09	0.10
Na2O	11.10	10.13	0.00	0.02	0.03	-	0.02	0.03
K2O	0.04	0.05	0.02	0.02	0.47	-	5.31	0.13
P2O5	-	-	0.01	0.03	0.06	-	0.01	0.00
SrO	0.35	0.42	0.31	0.37	0.20		0.32	0.05
NiO	-	-	-	-	-	0.01	-	-
ZnO	-	-	-	-	-	0.01	-	-
BaO	0.04	0.12	0.06	0.02	0.08	-	0.09	0.00
Cr2O3	0.00	0.02	0.03	0.04	0.00	0.04	0.12	0.05
V2O3	0.00	0.01	0.10	0.00	0.00	-	0.04	0.03
Total	99.38	100.23	97.06	96.86	86.74	95.01	95.36	88.39

Stilpnomelane is iron-rich with (26.53 wt%) FeO, moderate MgO (5.93 wt%) and contains negligible K_2O.

Magnetite shows typical compositions, with a high FeO content (94.51 wt%) and a closure of 95%, indicating the presence of trace elements.

Muscovite displays an unusual or altered chemical composition compared to common muscovite compositions reported in Fleet (2003). It is high in SiO_2 (55.29 wt%), FeO (4.45 wt%) and MgO (4.46 wt%) and low in Al_2O_3 (36.34 wt%) and K_2O (5.31 wt%).

Chlorite displays moderate SiO_2 (28.09 wt%) and is rich in FeO (20.27 wt%) and MgO (19.68 wt%).

7 Results

7.1 Thermodynamic Modelling

A pseudosection was calculated for sample RE2439 using the bulk rock composition of the type 1 domain. It displays mineral assemblages developed during the Alpine evolution and contains no relics of the early magmatic history (e.g., large plagioclase crystals with oscillatory zoning marked by inclusion trails, as observed in the type 2 domain). In detail, this domain contains sodic amphibole (Fe-glaucophane and riebeckite), albite, titanite, epidote, and magnetite. Rare stipnomelane replaces sodic amphibole and thus forms during the retrograde evolution.

Calculations were performed between 4–12 kbar and 350–500°C. The T interval was chosen based on the maximum T estimates from Raman spectroscopy of carbonaceous material in the Rechnitz Window (i.e., 422°C), recently obtained by the Berlin group. This provides the maximum T reached by the sample but does not indicate when this T is attained during the P–T evolution (i.e., pre- or post-peak-P conditions). The resulting pseudosections (Figure 24) produced 96 fields with stable mineral assemblages.

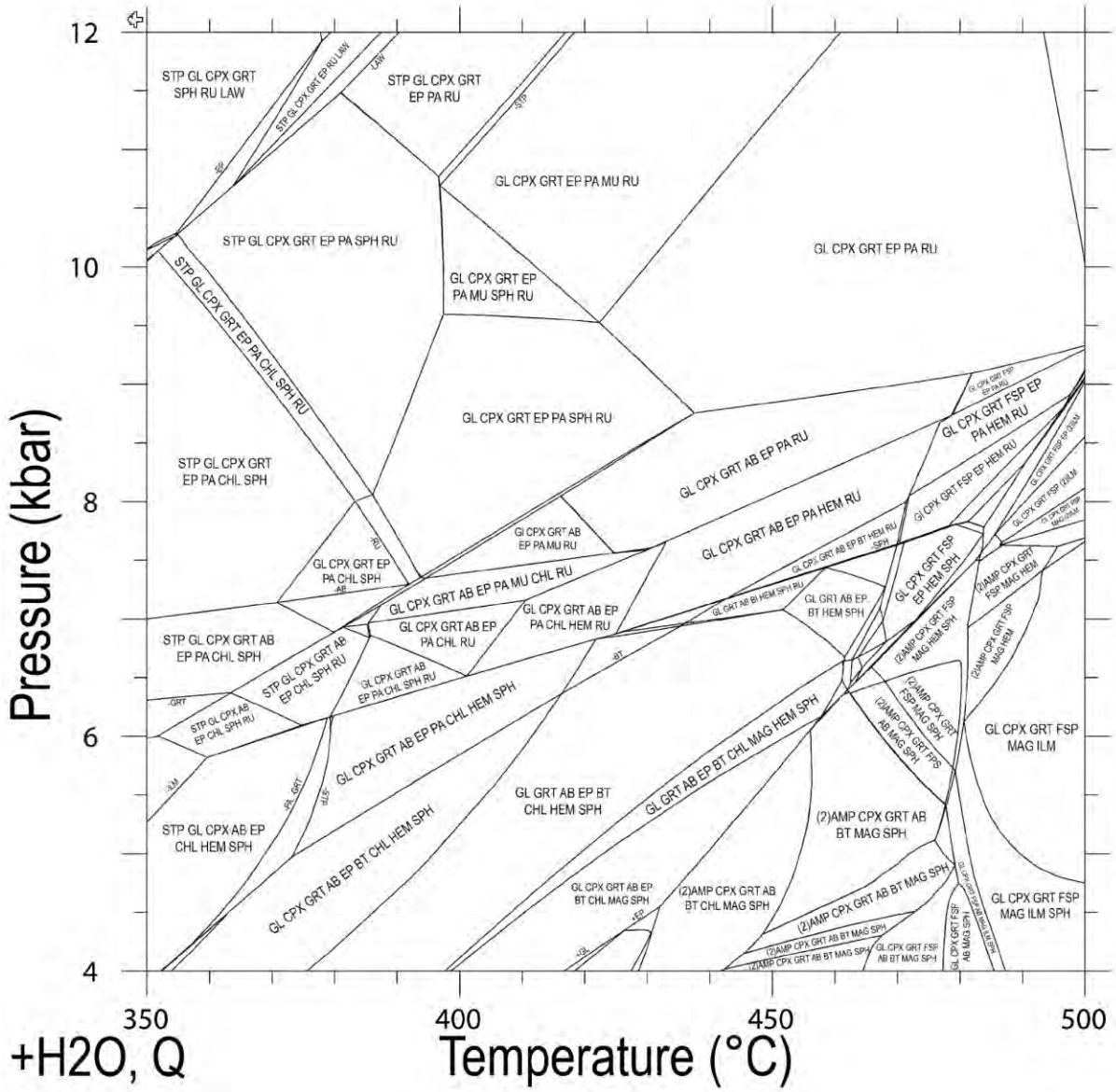

Figure 24: Pseudosection for RE2439 calculated using the bulk rock composition of domain 1. Fields display their stable mineral assemblage. The phases that appear or disappear are reported along the lines on the side of the affected field (i.e. +GRT would be in the field with garnet, -STP in the field where it is now absent). Mineral abbreviations used are Ab = albite, 2Amp = two amphiboles (Na, Ca) Bt = biotite, Chl = chlorite, Cpx = clinopyroxene (acmite, omphacite, see table 3), Ep = epidote, Fsp = feldspar, Gl = glaucophane (i.e. blue amphibole), Grt = garnet (spessartine, grossular, almandine, see table 3), Hem = hematite, Ilm = ilmenite, Law = lawsonite, Mag = magnetite, Mu = muscovite, Pa = paragonite, Ru = rutile, Sph = sphene (titanite), Stp = stipnomelane.

This diagram shows the mineral assemblages stable in the investigated P–T range, but it does not provide information on their modal abundances. The program TheriakDomino has been used to check the modal amount of the minerals in the fields of interest. Some of them are reported in Table 3. For instance, garnet is almost always present in the investigated P–T space, but its modal amount is very low (< 1.5 vol%, Table 1) and reaches 2.4 vol% only at 12 kbar and 500°C.

Similarly, the thermodynamic model predicts fields that contain biotite or muscovite (Figure 25b). However, their modal amount is also very low (<0.3 vol%; Table 3). These examples show that the imperfect match between thermodynamic predictions and petrographic observations can be attributed to the presence of a mineral in very small amounts that may not be detected in the thin section during petrographic investigation. It is generally assumed that the absence of a mineral, which is predicted by thermodynamic modelling in a limited modal amount, can be explained by the attainment of the 0.5 vol% threshold, below which a mineral is undetectable in thin section (Nagurney et al., 2021). In the following, these points will be considered to establish the P–T conditions reached by the sample under investigation.

Table 3: displays modal abundances of selected minerals as predicted by thermodynamic modelling.

T(°C) P (kbar)	350 4	400 4	450 4	500 4	350 6	400 6	450 6	500 6	350 8	400 8
garnet										
vol%	0	1	1.5	0.6	0	0.4	1.3	0.2	0.7	0.9
composition						*spss*	*grs*	*spss*	*spss*	*spss*
muscovite										
vol%	0	0	0	0	0	0.2	0	0	0	0
paragonite										
vol%	0	0	0	0	0.2	0	0	0	12	11
clinopyroxene										
vol%	8	7	5	11	17	4	0	15	14	13
composition	*acmite*	*omphacite*	*omphacite*	*omphacite*	*acmite*	*acmite*		*omphacite*	*acmite*	*acmite*
biotite										
vol%	0	0.2	0.2	0	0	0	0.3	0	0	0

T(°C) P (kbar)	450 8	500 8	350 10	400 10	450 10	500 10	350 12	400 12	450 12	500 12
garnet										
vol%	0.9	0.5	0.7	1	1.2	1.9	0.8	1	1.3	2.4
composition	*spss*	*grs*	*spss*	*spss*	*spss*	*alm*	*spss*	*spss*	*spss*	*alm*
muscovite										
vol%	0	0	0	0.03	0	0	0	0	0.02	0
paragonite										
vol%	0	0	15	7.9	7.9	0	0	6	7	8
clinopyroxene										
vol%	4.8	16.5	15	15	17	19	19	17	16.9	19
composition	*acmite*	*acmite*	*acmite*	*acmite*	*acmite*	*acmite*	*acmite*	*acmite*	*acmite*	*acmite*
biotite										
vol%	0	0	0	0	0	0	0	0	0	0

In the following Figures 25-31, the small phase diagram in the top part of the figure shows the P-T space (depicted in green) where the specific mineral assemblage discussed is stable. Red fields (i.e., fields excluded from the possible PT space) will increase progressively as more minerals are included in the discussion. This approach is applied to each mineral component of the peak mineral assemblage, allowing the P–T conditions under which it formed to be defined.

In the sample investigated, albite is one of the most abundant minerals. Thermodynamic modelling predicts the occurrence of albite at P < 9 kbar at ~470 °C and < ~7 kbar at 350 °C (Figure 25a). Paragonite, together with muscovite (both not observed in thin section), is predicted to be stable at higher pressures (see Figure 25b). A few fields at low P (<8 kbar) also contain paragonite, but at these conditions, its modal amount is almost 0% (see Table 3). These observations constrain the mineral assemblage to below 8 kbar.

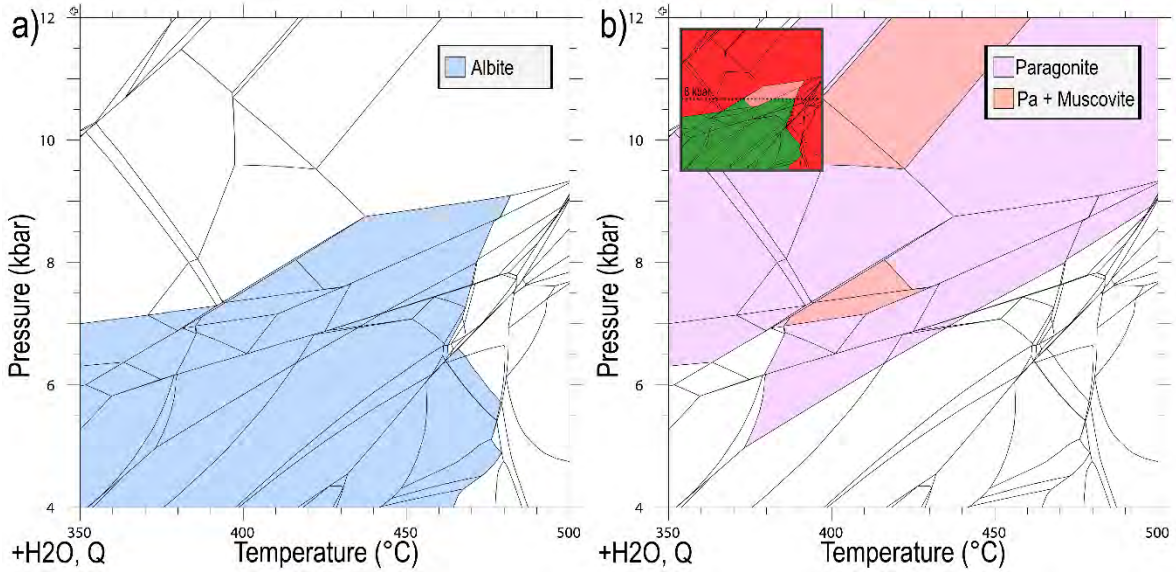

Figure 25: Displays the stability of albite a), and paragonite and muscovite b). In the top right, a small diagram will continuously be adjusted in green (possible fields for formation of the sample) and red (not possible due to mineral assemblage). In this figure, fields above 8 kbar, highlighted in light red, indicate where paragonite is stable in greater amounts.

Sodic amphibole is stable in the entire investigated P–T space. The composition of the sodic amphibole changes from a riebeckite to a glaucophane at increasing P. In the diagram, riebeckite and glaucophane are shown as a single amphibole because a solid solution exists between them. With increasing temperature between 440-490°C at pressures between 4-7 kbar, two amphibole phases become stable: riebeckite and actinolite. This is shown in Figure 26. Since only one amphibole was observed, these fields are excluded from the possible P–T conditions experienced by the studied sample.

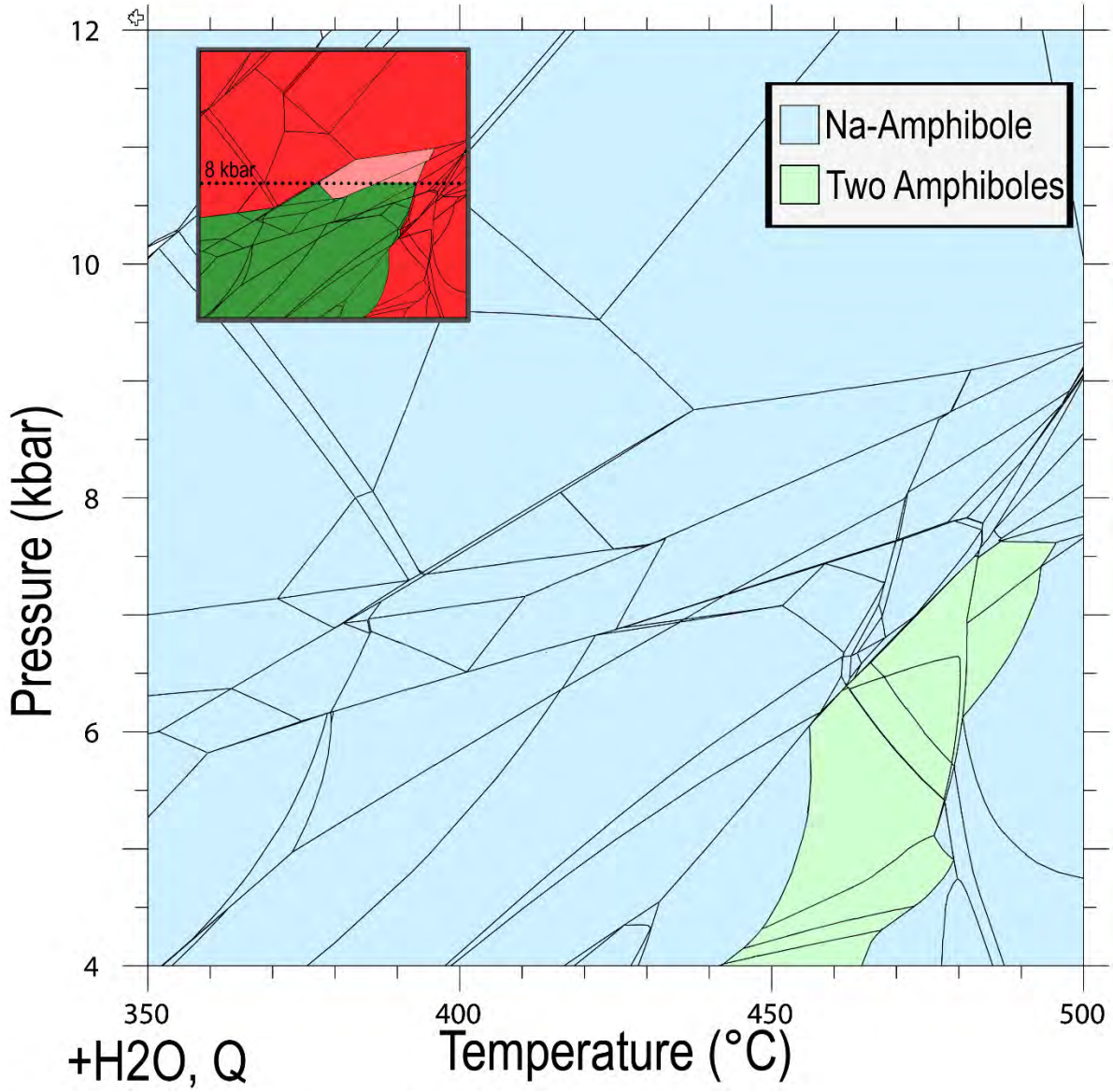

Figure 26: The stability of one amphibole (solid solution between riebeckite and glaucophane) and two amphiboles (riebeckite and actinolite)

Petrographic observations reveal that titanite occurs both as inclusions in sodic amphibole and as crystals in the matrix, defining bands oriented parallel to the main foliation. In the calculated diagram, titanite is stable over the entire P range at low T and over the entire T range at low P (Figure 27a). There are titanite-free fields in the centre of the P–T space between 4.5-8.5 kbar and 370-470°C in which albite is stable. Therefore, the absence of titanite helps to limit the P–T space for the observed mineral assemblage.

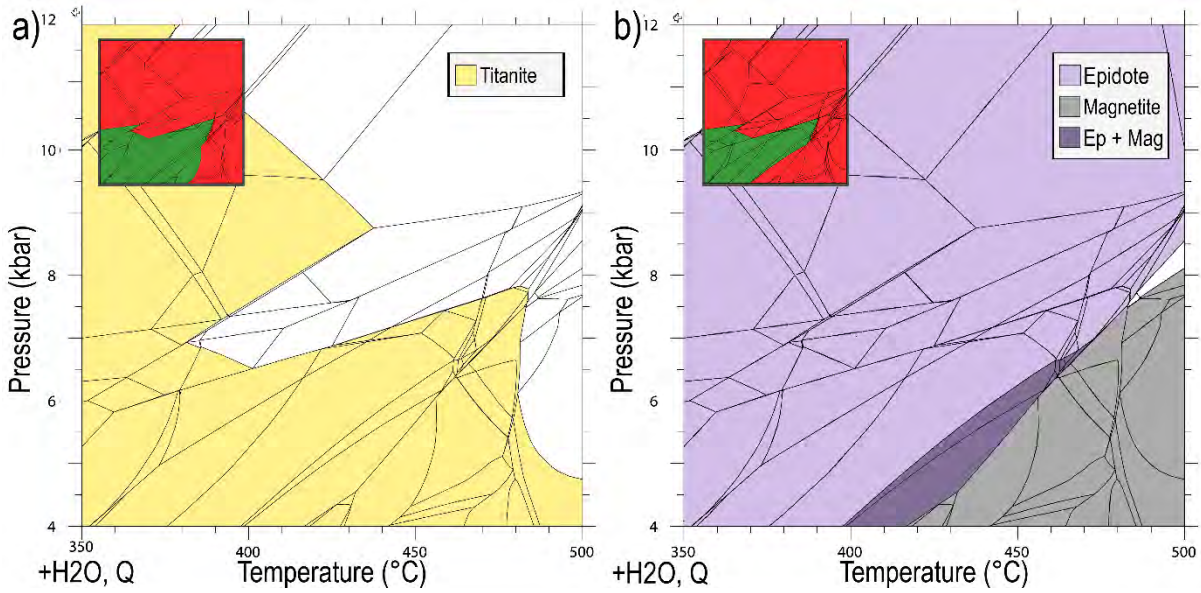

Figure 27: In this figure, the absence of titanite a) in fields where albite and paragonite are both stable limits the P–T space at which the observed mineral assemblage can be stable. On the right, epidote and magnetite further limit the area as they were abundant in the sample.

Epidote is quite abundant in the studied sample, and is modelled as stable over a very large part of the investigated P–T range, except for the right P–T corner (T >400 °C, P <8 kbar). The absence of epidote is counterbalanced by the presence of magnetite (Figure 27b). These two minerals coexist only in a very narrow P–T range, comprising 4 and 8. Kbar and 400–500 C°.

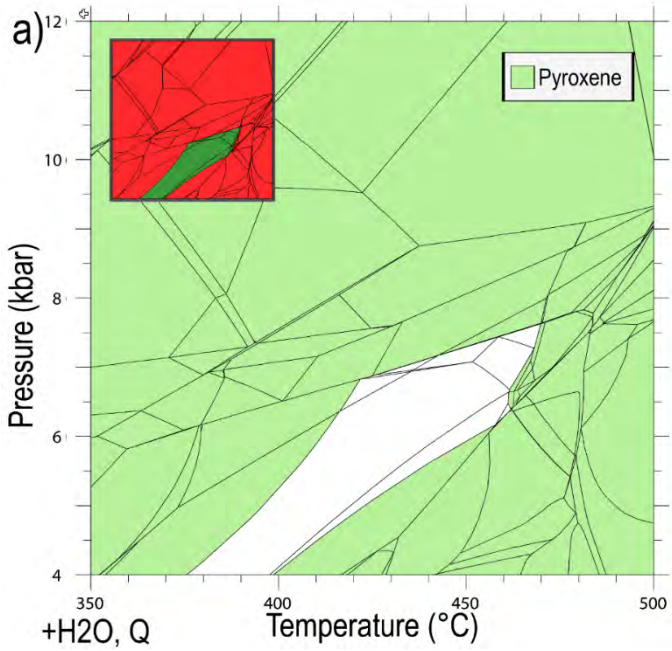

Figure 28: Pyroxene stability significantly reduces the fields and defines the final geometry of the pseudo-section.

Pyroxene was not observed under the microscope, neither as relic inclusions in the amphibole nor in the matrix. This drastically limits the number of remaining fields to eight, as pyroxene is stable under all conditions except for a small number of fields below 4-7 kbar and 360-470°C (dark-green field in the inset in the Figure above. The dark-green field comprises fields that contain the observed mineral assemblage albite-sodic amphibole-epidote-titanite-magnetite. In addition, some other minerals are present as discussed below.

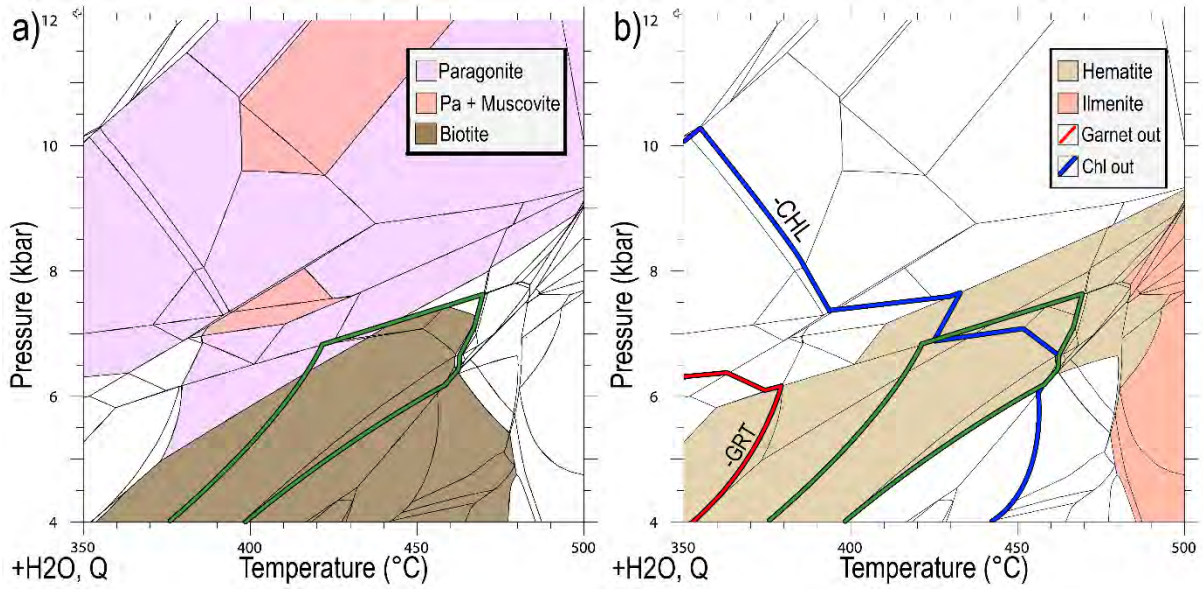

Figure 29: a) shows the stable micas in the pseudosection. In the relevant fields (within the green line), all can be disregarded due to their too-low modal amount. b) shows hematite and ilmenite fields, as well as grt-out and chl-out lines with the mineral abbreviation on the side where the phase is absent.

In Figure 29, the fields that contain the observed mineral assemblage are limited to within the green line. Their modal amounts generally agree with those estimated by Photoshop point counting. In Figure 29b, the garnet-out and chlorite-out lines are depicted in red and blue, respectively. In addition, the fields where hematite and ilmenite are present are coloured in brown and pink, respectively. Figure 30 shows the modal amounts of all stable minerals at certain P–T conditions within the P–T space delimited above. This information is used below to refine the P–T conditions of the mineral assemblage observed in the studied sample.

According to the diagram's topology, the fields bounded by the green line also contain the following minerals: paragonite, biotite, garnet, hematite, and chlorite. None of these minerals were detected during petrographic investigations. The modal amounts of paragonite and biotite are always very low (< 0.5 vol% threshold, below which a mineral is undetectable in thin section). The modal amount of garnet is low (< 1 vol%), and thus, it is possible that the mineral was not detected. By contrast, the modelling predicts that the chlorite modal amount can reach 3.9 vol% - an amount that would not go unnoticed under the microscope.

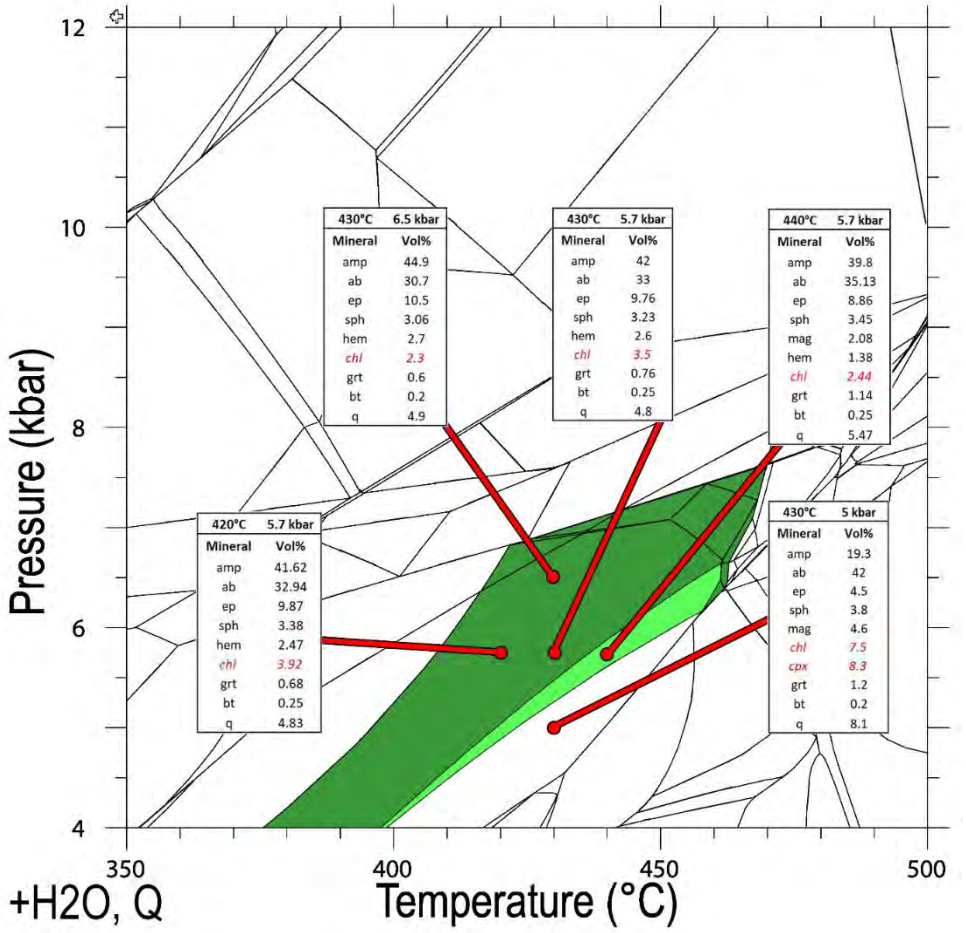

Figure 30: calculated modal amounts for relevant points.

Less puzzling is the existence of hematite. In reflected light microscopy, thin sections must be freshly polished with diamond grit to remove oxidised layers and reveal the minerals' colour, which is essential for identification. Because this could potentially alter chemical analyses at the microprobe, samples were not freshly polished, and opaques were oxidised. It is, thus, possible that not all opaques were magnetite, though hematite is strongly anisotropic in XPL as opposed to magnetite. It is conceivable that both phases are present, especially considering the low modal amount of hematite.

Despite the uncertainties of the modelling, petrographic observations and thermodynamic modelling suggest that the observed mineral assemblage sodic amphibole (Fe-glaucophane and riebeckite), albite, titanite, epidote, and magnetite grew at ~4-6.5 kbar and 395-460°C.

Finally, blue amphibole is partially replaced by stipnomelane. This mineral stabilises at T < 370°C and P < 8 kbar (Figure 31).

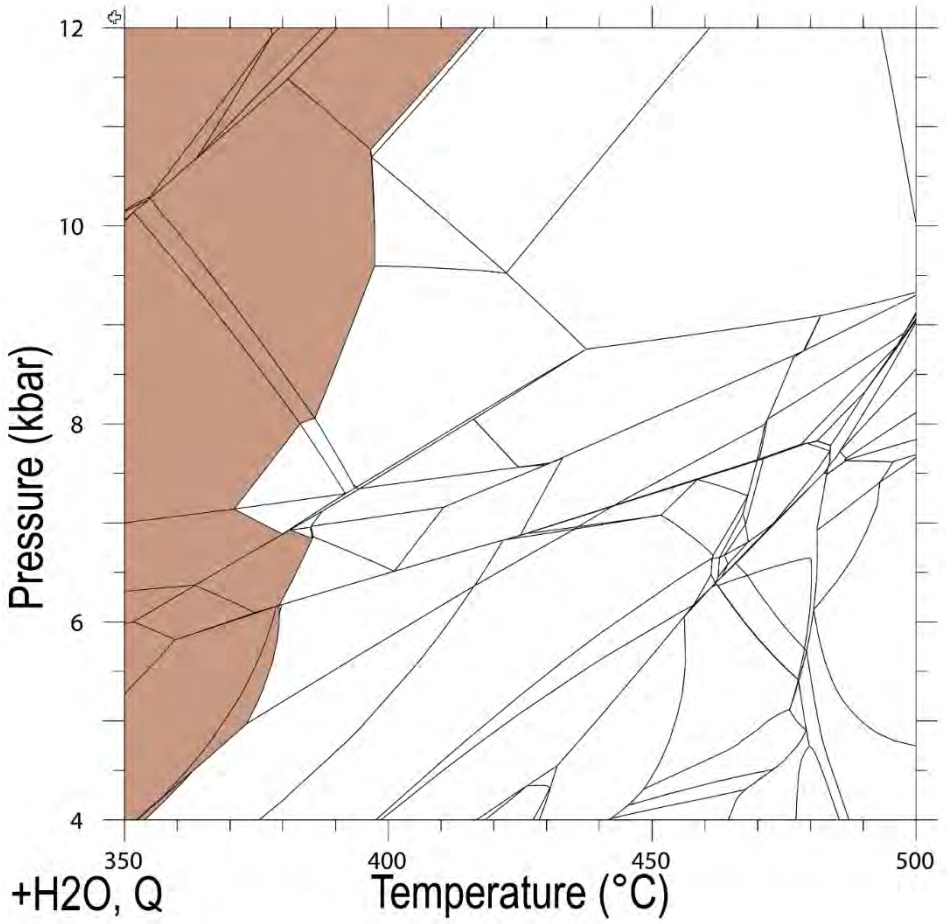

Figure 31: Stipnomelane is the only observed retrograde mineral with a clear pseudomorph geometry. Chlorite was not observed in this sample.

8 Discussion

This thesis aims to constrain the PT space at which samples from the Rechnitz Window have formed. This is achieved by constructing a pseudosection to define fields in a PT space that support the stable mineral assemblage in the sample. Samples were collected (by the Berlin group and Professor Manzotti), and thin sections were prepared and petrographically analysed. After that, whole-rock geochemical and mineral chemistry analyses were carried out. Using insights from the previous steps, a pseudosection was constructed, and potential fields for PT conditions were defined.

8.1 Sample preparation

Several samples were available for this thesis. Four plagiogranite samples were collected and prepared by the Berlin group. Here, only thin sections were available. The remaining two plagiogranites were collected and initially cut and prepared for thin section by Professor Manzotti. Two more greenschist samples, also collected by the Berlin group, had pre-prepared thin sections. Samples prepared in full by the Berlin group were used only for petrographic analyses under the microscope. This is because there was no available information about how they were cut. This means that, though in thin section they appeared to have been cut perpendicular to the foliation, this could not be guaranteed.

By contrast, samples prepared “in-house”, such as RE2439a, RE2439b, RE40 and RE46, could be used for these chemical analyses and were prepared specifically for this thesis. As such, it could be ensured that thin sections were cut perpendicular to the foliation. For whole-rock geochemistry analyses, great care was taken to remove rust stains from the samples before crushing. The rock saw, using a 3mm-thick blade, removes material with each cut. This means that with each cut, material is lost. Because of this, a compromise between material loss and rust removal had to be reached. Great care was also taken to isolate the different domains and not include part of one in the other.

8.2 Whole Rock Geochemistry

In this thesis, plagiogranite is compared with samples from previous studies, and whole-rock geochemical similarities are observed. Firstly, Type 1 and Type 3 domains (blue rectangles), together with the average composition of plagiogranite (red triangle), generally plot closely with Koller's (1985) blueschist samples; see, for example, Figure 18.

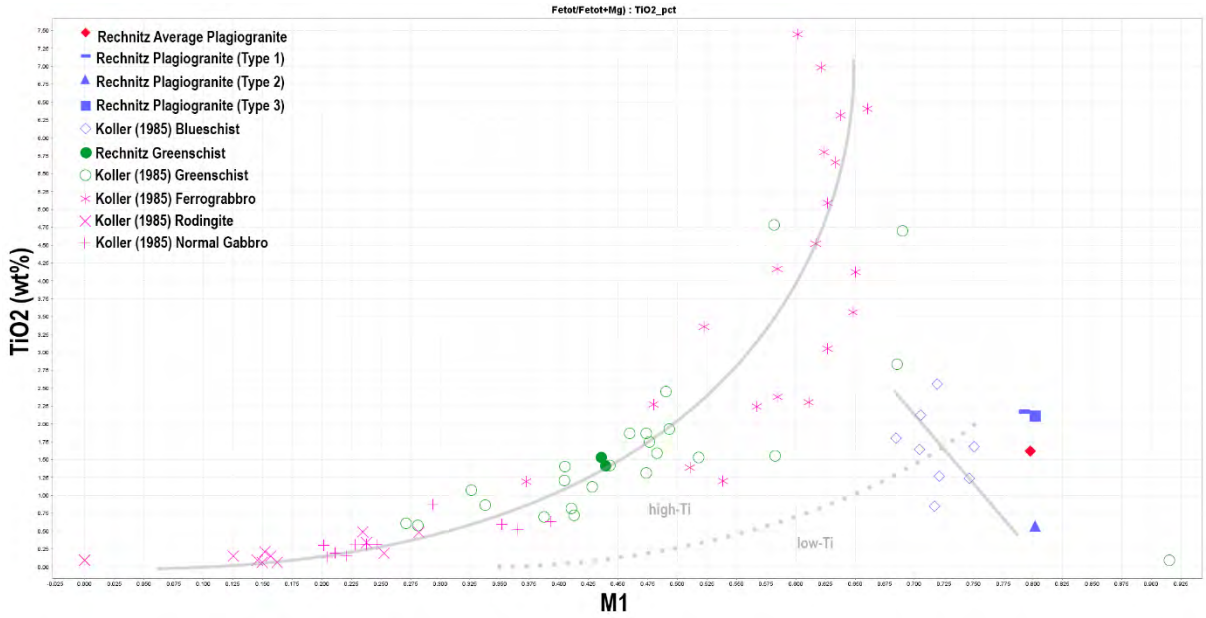

Figure 32: The figure shows the fractionation trend discussed in detail above.

When considering M1 vs Ti in the Figure above, however, the average composition of sample RE2439 plots with lower titanium and higher M1 than Koller's samples. Moreover, the frequently observed pyroxene in Koller's samples was never observed in any of the samples within this thesis, despite some of them being collected in the same area. This suggests that the plagiogranites in this thesis and the blueschists in Koller (1985) may represent different rock types or have undergone different metamorphic processes. As for the latter, this would require that all pyroxenes were fully replaced by amphiboles in the investigated rocks, without leaving pseudomorph geometries. To better understand these options, additional whole-rock geochemical analyses of other samples would be needed. This would allow for a more detailed comparison of chemical differences, such as the lower Mg# of RE2439, and provide a deeper understanding of whether this is an exception or the norm.

The type 2 domain plots alongside acid rocks from Ohnestetter et al. (1981) and one of Koller's (1985) samples. Both Koller and Ohnestetter et al. (1981) describe these samples as albite-rich veins (see Koller 1985) or as rocks containing up to 80% albite (see Ohnestetter et al. 1981). This is in line with the domain-specific description of the Type 2 domain in this thesis and explains the good agreement observed. Ohnestetter et al. (1981) concluded that a high-density, iron-rich liquid and a low-density, silica-rich liquid formed. As these two magmas don't mix, the latter rapidly rises, forming the "acid rocks" (i.e. plagiogranites). This is confirmed and elaborated on by Koller (1985), who identifies that the "*albite-rich veins in blueschist (...) represent those fractionated products of the magma chambers with the highest degree of differentiation*". And indeed, this is confirmed by domain-specific analyses in this

thesis. The Type 2 domain (blue triangle in Figure 33), which corresponds to the albite-rich veins described by Koller (1985), plots in close agreement with acid rocks (i.e., plagiogranites) from Ohnestetter et al. (1981), confirming the claim above.

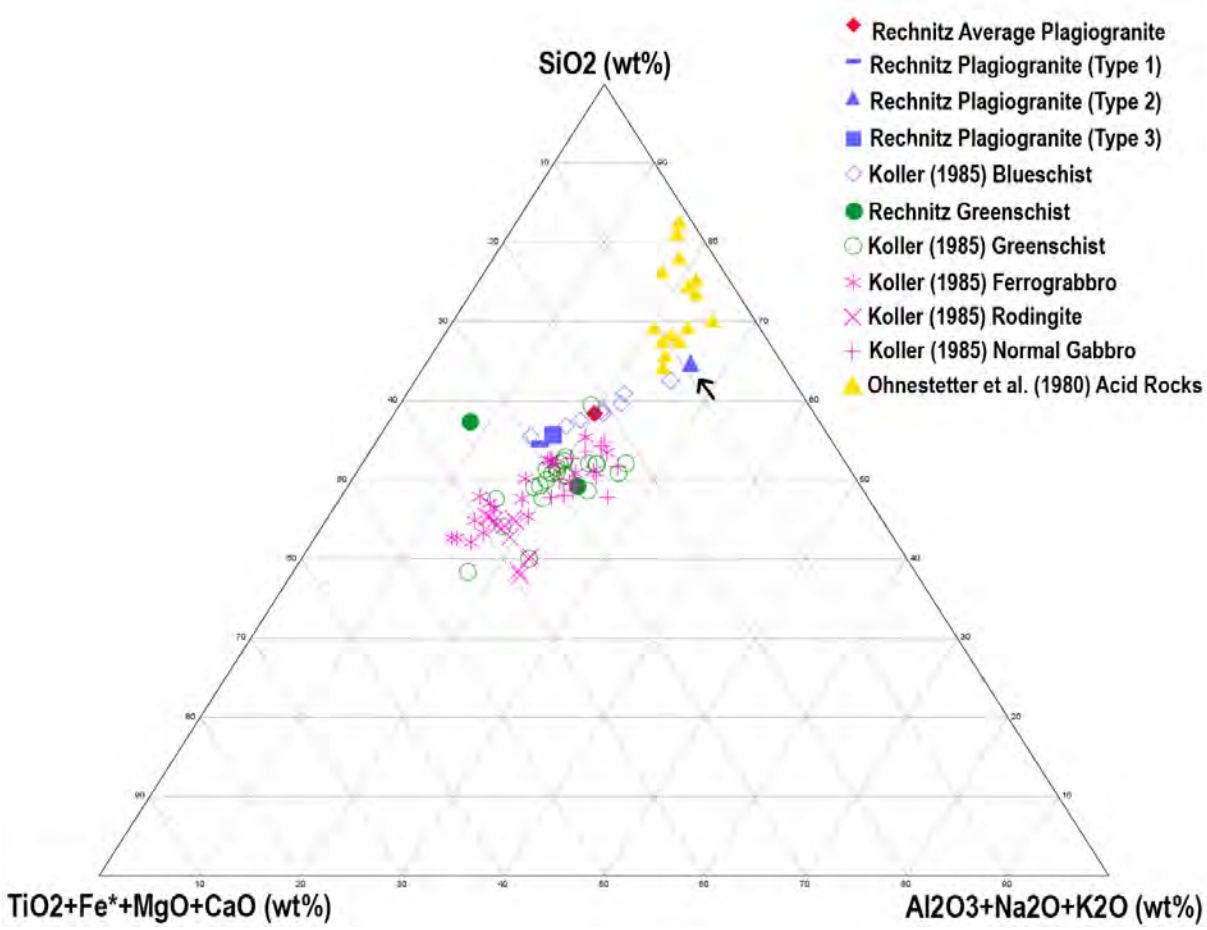

Figure 33: Ternary diagram comparing all the samples discussed.

Greenschist sample RE46 plots in good agreement with greenschists from Koller (1985). Sample RE40 shows significantly lower Al_2O_3 and slightly lower K_2O and, as a result, plots outside the greenschist cluster in the ternary diagram in Figure 33. Differences in Fe_2O_3 are likely caused by rust. Here, despite being more rust-coated from the outside, sample RE40 displayed lower amounts than RE46. This is because sample RE40 was more compact with only a few rust-filled fractures, while RE46 contained more cracks and pits. Despite best efforts to remove rust, some likely remained in the sample before analysis.

8.3 Mineral Chemistry

Analysed S1 and S2 amphibole crystals displayed great chemical variability between Fe-glaucophane and riebeckite, with no clear core-to-rim zoning pattern as highlighted in Figure 22. By contrast, chemical variation appears more random. Here, as seen under the microscope, lighter blue corresponds to riebeckite compositions, while darker shades are Fe-glaucophane. As for the chemical variability, a sampling bias appears likely. Due to time constraints at the microprobe, six sites were selected for analysis: three sites contain blue

amphibole marking the S1 foliation, and three sites contain blue amphibole defining the S2 foliation. Here, the aim was to check if different shades of blue, as well as S1 vs S2 orientation, correspond to different chemical compositions. Logically, zoned crystals were preferentially selected. Only one crystal returned values with no large chemical variability. It is therefore possible that if crystals were more randomly selected, a greater intra-crystal chemical homogeneity would become visible, though this would not meaningfully change the results from this thesis's main focus, the Type 1 domain PT analyses.

Surprisingly, all amphiboles measured in sample RE46 returned chemically homogeneous, actinolite compositions. This is especially puzzling, as the analysed crystals were selected based on their varying optical properties (interference colour, shape, and size). The most likely explanation for this is a more complex crystal orientation relative to the foliation. In other words, crystals that appear perfectly parallel to, or 90° offset from, the foliation might in reality be slightly rotated and therefore cut at an angle. This could explain differences in appearance under the microscope despite similar chemistry. To resolve this, more chemical analyses would be required.

Originally, under the microscope, some feldspar crystals appeared to exhibit tartan twinning – meaning they were interpreted as potassium feldspar relicts. All analysed feldspars, including those with suspected tartan twinning, returned albite compositions. Tartan twinning is a combination of albitic twinning and pericline twins at a monoclinic to triclinic transition. They are most common in microcline but can rarely occur in albite, explaining the initial confusion (Nespolo and Souvignier, 2025).

As explained earlier, epidote and titanite are very difficult to distinguish in thin section when not included with amphibole. As the microprobe analyses showed, all larger, sheet-like inclusions in amphibole were titanite. Even matrix crystals with higher interference colours, similar to those of epidote, returned titanite values. This makes point counting extremely challenging and likely led to an over- or underestimation of either phase. Zoned and twinned crystals, by contrast, were all epidote. This means that at least one of the two properties is needed to distinguish them at the microscope without chemical analyses. This, however, was not often the case.

A large area of uncertainty is opaque minerals, specifically magnetite and hematite. All crystals were analysed with the microprobe and returned magnetite signatures (high FeO at 95% and closure around 95%). It is important to note that these analyses were performed before the thermodynamic modelling. As a result, only a few crystals were checked as they were all assumed to be magnetite based on microscopy. In thin section, a handful of opaques displayed slightly different characteristics, though no anisotropy was observed, which would be required for hematite. It is certainly possible that a small amount of hematite remains hidden in the thin section and was missed even after rechecking following the modelling. Another possibility is erroneously high Fe^{3+} values, which are discussed in more detail below.

8.4 The growth of sodic amphibole

In the Rechnitz Window, sodic amphibole is found in the rare plagiogranite (this thesis) and blueschist lenses (Koller, 1985). Studies such as Evans (1990) have found that the stability field of sodic amphibole is increased by high Fe^{3+} and low-Al environments. Manzotti et al. (2020) reported similar effects in low-Mg# i.e., Mg/(Mg + Fe^{2+}) and high-Na_2O environments. Moreover, environments with high Fe^{3+}/Fe_{tot} combined with low Mg# also favour the growth of sodic amphibole. Therefore, the chemical conditions in the Rechnitz Window that favoured the growth of sodic amphibole can be identified by analysing these ratios.

As shown in Figure 34, all plagiogranites from this thesis and the blueschists in Koller (1985) contain sodic amphiboles, indicated by filled symbols. For both groups, the Mg# is lower than in the greenschists, while Na_2O is significantly higher. Similarly, though not as markedly different as sodium, the Fe^{3+}/Fe_{tot} ratio, averaging around 0.35, is also higher than in the greenschist. Based on this, it appears that the conditions for the growth of sodic amphibole were ideal in the plagiogranites, considering the low Mg#, the high Na and the relatively high Fe^{3+}/Fe_{tot}. Two outliers, highlighted with a red arrow, nicely illustrate this point. Koller's (1985) sample RS-58/78 has an Mg# vs Fe^{3+}/Fe_{tot} ratio at which sodic amphibole already appears in the plagiogranites. Yet, considerably lower Na values appear to have hindered the growth of sodic amphibole in this sample. Similarly, sample RS 18/77 has both too-low Mg# relative to Fe^{3+}/Fetot and Na_2O ratios that are too low for sodic amphibole to form.

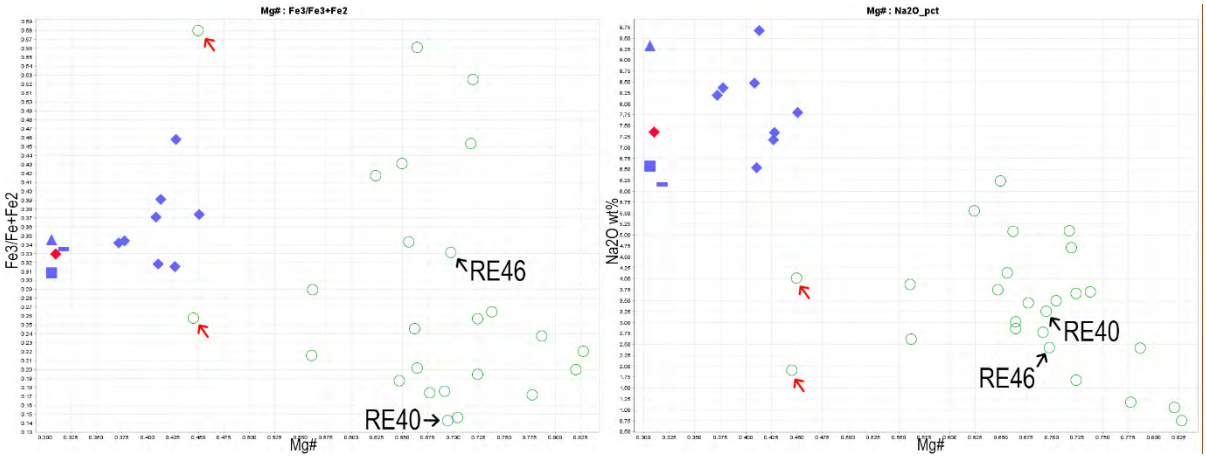

Figure 34: diagrams showing Mg# vs Fe^{3+}/Fe_{tot} and Mg# vs Na_2O, i.e. sodic-amphibole controlling chemical environments. In this figure, filled symbols indicate sodic amphibole-containing rocks, and hollow symbols indicate sodic amphibole-free rocks. The outliers are highlighted with a red arrow.

8.5 Thermodynamic Modelling and PT

In this MSc thesis, for the first time, thermodynamic modelling is used to constrain the peak P–T conditions reached by the Rechnitz Window. This approach constrains the observed mineral assemblage sodic amphibole (Fe-glaucophane and riebeckite), albite, titanite, epidote, and magnetite at ~4-6.5 kbar and 395-460°C. These P–T conditions only marginally overlap with those suggested by Koller (1985). Compared to the eoalpine peak-P metamorphic event (6-8

kbar and 330°C-370°C), there is only minimal pressure overlap, while the temperature does not overlap at all. Koller (1985) associates this stage with the growth of clinopyroxenes, hematite, magnetite, stipnomelane and albite. Compared to the conditions during the neoalpine metamorphic event, <3 kbar and 390-430°C, almost complete T-overlap is observed, but pressure results are far too high. This stage is associated with the growth of clinopyroxene, riebeckite to Mg-riebeckite, biotite, chlorite, epidote, magnetite, pyrite and titanite. Koller's (1985) very low-pressure estimates are based on the coexistence of Na-amphiboles and pyroxenes with a jadeite component of less than 5%. This coexistence was never observed.

By contrast, the T estimated by the Berling group (~420°) using the Raman spectroscopy on carbonaceous material matches the one estimated by thermodynamic modelling in this thesis well. There are some uncertainties in the thermodynamic modelling, as described in the section above. The main discrepancies are the presence of minerals not observed under the microscope. One of these is garnet, which is present in a low modal amount. The presence of this mineral in the modelled pseudosection can be linked to the fact that there is too much MnO in the bulk, which stabilises garnet (one of the few minerals that can incorporate MnO as Nagurney et al. (2021) argue). The presence of MnO in the sample requires the formation of garnet as the only stable phase capable of accommodating this component, albeit at very low modal amounts. Because of this, it can be considered absent for microscopy.

As already mentioned above, it is possible that hematite was missed in the analyses. Another possibility is that the Fe^{3+} content used for the modelling was too high, enlarging the stability field of hematite and other Fe^{3+}-rich minerals, such as clinopyroxene. The method used to estimate the Fe^{3+} content of the rock yields the maximum Fe^{3+} content. However, weathering and post-peak-P–T processes can further increase the Fe^{3+} content. This would result in the erroneous assumption that hematite was stable, when in reality it was not. In the modelling, the solid-solution models for amphibole, clinopyroxene, biotite, garnet, epidote, magnetite, and ilmenite–hematite incorporate Fe^{3+}. Especially at the greenschist-to-blueschist transition, the effect of Fe^{3+} on amphibole, clinopyroxene, and hematite is profound (Manzotti et al. 2020). For instance, in most fields, the modelled clinopyroxene corresponds to acmite, an Fe^{3+}-rich clinopyroxene. As shown by Diener and Powell (2010), the coexistence of glaucophane and hematite requires very high Fe^{3+} conditions. In the calculated pseudosection, these two phases are stable in many fields at low P, suggesting that the Fe^{3+} content is very high. In order to address this point, isothermal P–X(Fe_2O_3) phase diagrams (at peak T conditions, 420–450 °C) should be calculated, allowing for the estimation of how the change in Fe^{3+} in the bulk affects the appearance of Fe^{3+}-bearing minerals (hematite, acmite) and eventually the peak P–T conditions.

9 Conclusions and future perspectives

The petrographic observations, whole-rock and mineral chemistry, thermodynamic modelling, and the constructed pseudosection suggest that sample RE2439 formed at ~4-6.5 kbar and 395-460 °C. This is in good agreement with the results from the Berlin group (422°C) but is at odds with the stages defined by Koller (1985) and the reported pressure and temperature values. Koller uses the coexistence of pyroxenes with sodic amphiboles to constrain the pressure for the last metamorphic event (<3 kbar), but these pyroxenes were never observed. This calls into question the applicability of this pressure value to the samples investigated in this thesis, despite the proximity of their collection sites. Here, additional samples must be collected to identify the much-described pyroxenes and construct a pseudosection of a sample containing this phase. The absence of pyroxenes from the samples in this thesis, and the implications thereof, remain an area of interest that this thesis cannot address.

Chemically, the type 1, type 3, and average domain plots are in close agreement with those of Koller (1985). To address discrepancies, such as the significantly lower Mg#, significantly more samples should be analysed. The type 2 domain described in this thesis, by contrast, agrees nicely with Koller (1985) and Ohnestetter et al. (1981) and describes a fractionation product.

The erroneously high Fe^{3+} and the implications of it for the construction of a pseudosection should be addressed by constructing a P–X(Fe_2O_3) pseudosection and investigating the changes of stability fields and the associated P-T values.

10 Acknowledgements

I want to thank my supervisor, Professor Paola Manzotti, for her patience, input, and guidance – not only during this Master's thesis but also during my Bachelor's thesis and the courses she taught over the years. I am grateful for her trust and for the extra learning opportunities I enjoyed as the teacher's assistant in seminars and on the field trip I was allowed to attend.

I also want to thank Professor Vicky Pease for her guidance and input regarding the interviews and transition to the industry.

Darüber hinaus danke ich meiner Familie (Eltern, Großeltern, liebe Stiefeltern, Frau und Kegel und Professor Freitag) für eure Unterstützung und eure Geduld auf meinem akademischen Weg. Und auch so im Leben ist es schön euch zu haben, das kann man ja ruhig mal gesagt haben.

Reference list

Ballèvre, M., Manzotti, P. and Dal Piaz, G.V. (2018). Pre-Alpine (Variscan) Inheritance: A Key for the Location of the Future Valaisan Basin (Western Alps). *Tectonics*, 37(3), pp.786–817. doi:https://doi.org/10.1002/2017tc004633.

Bourrouilh, R. (2012). The Aquitaine Basin and the Pyrenees: geodynamical evolution and hydrocarbons. In: *Regional Geology and Tectonics: Phanerozoic Passive Margins, Cratonic Basins and Global Tectonic Maps*. Elsevier.

Bucher, K. and Grapes, R. (2011). *Petrogenesis of Metamorphic Rocks*. Springer Science & Business Media.

Cao, S., Neubauer, F., Manfred Bernroider, Liu, J. and Genser, J. (2013). Structures, microfabrics and textures of the Cordilleran-type Rechnitz metamorphic core complex, Eastern Alps. *Tectonophysics*, 608, pp.1201–1225. doi:https://doi.org/10.1016/j.tecto.2013.06.025.

de Togni, M., Balestro, G., Rubatto, D., Castelli, D., Gattiglio, M. and Festa, A. (2024). Late Jurassic magmatism in the Ligurian-Piedmont Ocean constrained by zircon ages of mafic and felsic meta-intrusives. *Terra Nova*, 36(5), pp.403–413. doi:https://doi.org/10.1111/ter.12723.

Deer, W.A., Howie, R.A. and J Zussman (2013). *An introduction to the rock-forming minerals*. London: The Mineralogical Society.

Diener, J.F.A. and Powell, R. (2010). Influence of ferric iron on the stability of mineral assemblages. *Journal of Metamorphic Geology*, 28(6), pp.599–613. doi:https://doi.org/10.1111/j.1525-1314.2010.00880.x.

Eline Le Breton, Brune, S., Ustaszewski, K., Zahirovic, S., Seton, M. and R. Dietmar Müller (2021). Kinematics and extent of the Piemont–Liguria Basin – implications for subduction processes in the Alps. *Solid Earth*, 12(4), pp.885–913. doi:https://doi.org/10.5194/se-12-885-2021.

Evans, B.W. (1990). Phase relations of epidote-blueschists. *Lithos*, 25(1-3), pp.3–23. doi:https://doi.org/10.1016/0024-4937(90)90003-j.

Fleet, M.E. (2003). *Rock forming minerals. 3, Sheet silicates. A, Micas*. London: Geological Society.

Holland, T.J.B. and Powell, R. (2011). An improved and extended internally consistent thermodynamic dataset for phases of petrological interest, involving a new equation of state for solids. *Journal of Metamorphic Geology*, 29(3), pp.333–383. doi:https://doi.org/10.1111/j.1525-1314.2010.00923.x.

Hoogerduijn-Strating, E.H. (1991). *The evolution of the Piemonte-Ligurian ocean: a structural study of ophiolite complexes in Liguria (NW Italy)*. [online] Available at: https://research-portal.uu.nl/en/publications/the-evolution-of-the-piemonte-ligurian-ocean-a-structural-study-o/.

IMDEX (2019). *IMDEX | ioGAS™ Geochemistry Software*. [online] Imdex.com. Available at: https://www.imdex.com/software/iogas [Accessed 19 May 2026].

Koller, F. (1985). Petrologie und Geochemie der Ophiolite des Penninikums am Alpenostrand. In: *Jahrbuch der Geologischen Bundesanstalt*. Geologische Bundesanstalt Wien.

Locock, A.J. (2014). An Excel spreadsheet to classify chemical analyses of amphiboles following the IMA 2012 recommendations. *Computers & Geosciences*, 62, pp.1–11. doi:https://doi.org/10.1016/j.cageo.2013.09.011.

Manzotti, P., Ballèvre, M., Pitra, P., Putlitz, B., Robyr, M. and Othmar Müntener (2020). The Growth of Sodic Amphibole at the Greenschist- to Blueschist-facies Transition (Dent Blanche, Western Alps): Bulk-rock Chemical Control and Thermodynamic Modelling. *Journal of Petrology*, 61(4). doi:https://doi.org/10.1093/petrology/egaa044.

Manzotti, P. and Bellèvre, M. (2024). Continental Subduction in the Alps: from field data to kinematic models. In: *Geodynamics of the Alps*. Wiley, pp.255–313. doi:https://doi.org/10.1002/9781394299539.ch5.

Marton, E., Mauritsch, H.J. and Pahr, A. (1987). Paläomagnetische Untersuchungen in der Rechnitzer Fenstergruppe. *Mitteilungen der Österreichischen Geologischen Gesellschaft*, 80.

Nagurney, A.B., Caddick, M.J., Dragovic, B. and Busse, K. (2021). The (chemical) potential for understanding overstepped garnet nucleation and growth. *American Mineralogist*, 106(5), pp.812–829. doi:https://doi.org/10.2138/am-2021-7354.

Nespolo, M. and Souvignier, B. (2025). Structural analysis of twins in feldspars. II. Albite-pericline twinning and the metric pseudo-symmetry of feldspar lattice. *Mineralogy and Petrology*, 120(1), pp.161–185. doi:https://doi.org/10.1007/s00710-025-00950-0.

Nikolaus Froitzheim and Gianreto Manatschal (1996). Kinematics of Jurassic rifting, mantle exhumation, and passive-margin formation in the Austroalpine and Penninic nappes (eastern Switzerland). *Geological Society of America Bulletin*, 108(9), pp.1120–1133. doi:https://doi.org/10.1130/0016-7606(1996)108%3C1120:kojrme%3E2.3.co;2.

Ohnestetter, M., Ohnestetter, D., Vidal, P., Cornichet, J., Hermitte, D. and Mace, J. (1981). Crystallization and age of zircon from Corsican ophiolitic albitites: consequences for oceanic expansion in Jurassic times. *Earth and Planetary Science Letters*, 54(3), pp.397–408. doi:https://doi.org/10.1016/0012-821x(81)90056-x.

Piller, W.E. and Rasser, M.W. (2001). *Paleogene of the Eastern Alps*. Österreichische Akademie Der Wissenschaften.

Raith, M., Raase, P. and Reinhardt, J. (2012). *GUIDE TO THIN SECTION MICROSCOPY Second Edition*. [online] Available at: http://www.minsocam.org/msa/OpenAccess_publications/Guide_Thin_Sctn_Mcrscpy/Thin_Sctn_Mcrscpy_2_prnt_eng.pdf [Accessed 23 Sep. 2025].

Ratschbacher, L., Dingeldey, C., Miller, C., Hacker, B.R. and McWilliams, M.O. (2004). Formation, subduction, and exhumation of Penninic oceanic crust in the Eastern Alps: time constraints from 40Ar/39Ar geochronology. *Tectonophysics*, 394(3-4), pp.155–170. doi:https://doi.org/10.1016/j.tecto.2004.08.003.

Rosenbaum, G. and Lister, G.S. (2005). The Western Alps from the Jurassic to Oligocene: spatio-temporal constraints and evolutionary reconstructions. *Earth-Science Reviews*, 69(3-4), pp.281–306. doi:https://doi.org/10.1016/j.earscirev.2004.10.001.

Schmid, S.M., Fügenschuh, B., Kissling, E. and Schuster, R. (2004). Tectonic map and overall architecture of the Alpine orogen. *Eclogae Geologicae Helvetiae*, 97(1), pp.93–117. doi:https://doi.org/10.1007/s00015-004-1113-x.

Schönlaub, H.P. (2000). Burgenlad - Erläuterungen zur Geologischen Karte des Burgenlandes 1:200 000. *Geologische Bundesanstalt Wien*.

Science Education Resource Center at Carleton College (SERC) (2007). *What are Pseudosections?* [online] Teaching Phase Equilibria. Available at: https://serc.carleton.edu/research_education/equilibria/pseudosections.html.

Serri, G. (1981). The petrochemistry of ophiolite gabbroic complexes. A key for the classification of ophiolites into low-Ti and high-Ti types. *Earth and Planetary Science Letters*, 52(1), pp.203–212. doi:https://doi.org/10.1016/0012-821x(81)90221-1.

Stampfli, G.M., Mosar, J., Marquer, D., Marchant, R., Baudin, T. and Borel, G. (1998). Subduction and obduction processes in the Swiss Alps. *Tectonophysics*, 296(1-2), pp.159–204. doi:https://doi.org/10.1016/s0040-1951(98)00142-5.

Winter, J.D. (2014). *Principles of igneous metamorphic petrology*. Harlow: Pearson, Cop.

Yakymchuk, C. (2017). Applying Phase Equilibria Modelling to Metamorphic and Geological Processes: Recent Developments and Future Potential. *Geoscience Canada*, 44(1), p.27. doi:https://doi.org/10.12789/geocanj.2017.44.114.

Zhang, X., Liu, B., Wang, J., Zhang, Z., Shi, K. and Wu, S. (2014). Adobe photoshop quantification (PSQ) rather than point-counting: A rapid and precise method for quantifying rock textural data and porosities. *Computers & geosciences*, 69(69), pp.62–71. doi:https://doi.org/10.1016/j.cageo.2014.04.003.

Table of Figures

Appendix

Sample description

In the following, other samples of plagiogranite are described. In these samples, we did not perform mineral analyses and thermodynamic modelling.

RE10.2

This sample contains 70% blue amphibole, 26% albite and epidote, and magnetite at below 2%. The foliation in this sample is defined by the general orientation of small, prismatic, 0.2-mm-long blue amphiboles that weakly mark the S_2. The largest blocky crystals, exceeding 0.6 mm in size, are often offset up to 90° towards the foliation, suggesting the presence of an earlier relict S_1 foliation. In PPL, amphiboles range from pale blue to vibrant blue, with some crystals displaying patchy zoning between the two. Here, rims tend to be somewhat paler. While smaller crystals, especially those without inclusions, certainly exist, most amphiboles host numerous titanite inclusions with no clear core-to-rim trend. By contrast, in the cores of larger amphibole inclusions, zircon and titanite are found. Stilpnomelane, a rare accessory, appears to have fully replaced single, small amphibole needles.

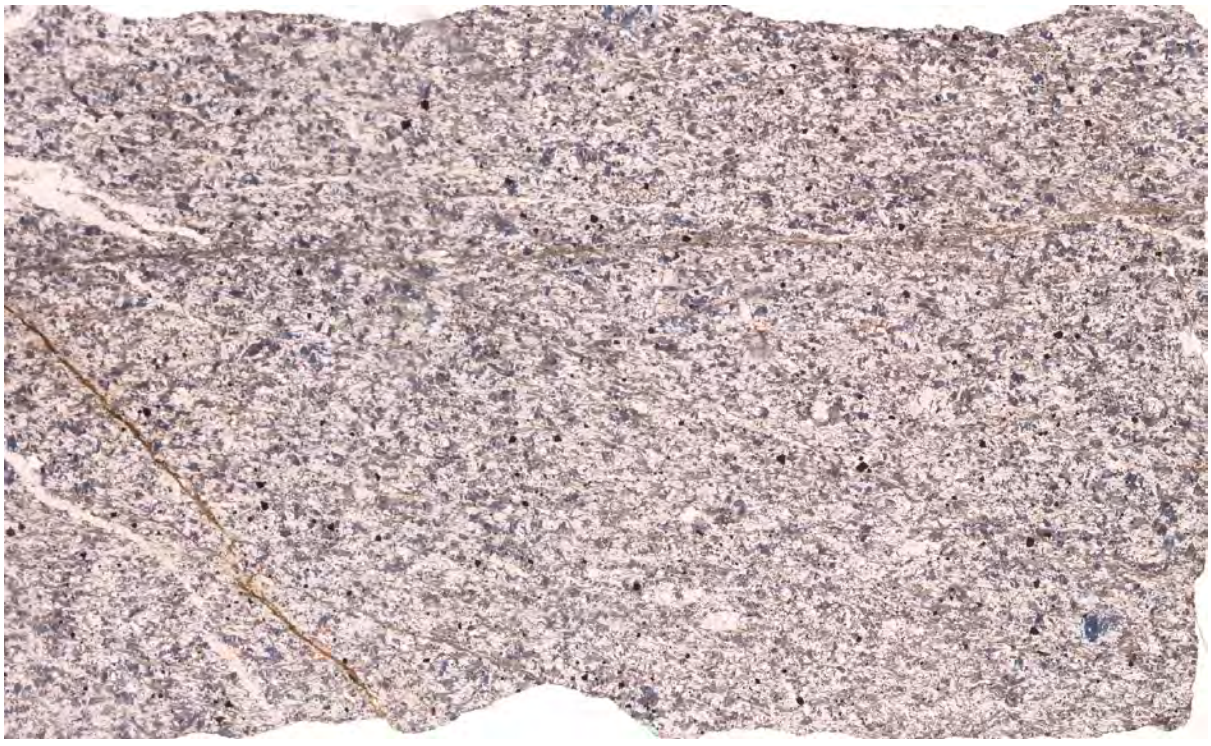

Figure 35: Thin section scan of sample RE10.2 (PPL).

Albite display either no twinning, polysynthetic twinning, or tartan twinning in single crystals. They range in size from <10 µm to 0.4 mm and have a clean appearance. Inclusions in the smaller crystals are generally limited to tiny green amphibole needles in random orientations and single rounded grains of epidote. The largest crystals are significantly more inclusion-rich, often displaying oscillatory rings with varying degrees of inclusions that suggest previous

growth stages. These inclusions consist of tiny grains of epidote and green amphibole. Areas with larger crystals that began to recrystallise are inclusion-free.
Beyond the microscopic inclusions in plagioclase, epidote is a rare accessory in this sample, with only individual crystals. These display slightly yellow pleochroism and neon-blue cores that transition to purple towards the rim. A vein filled with opaque material (Figure XXX) crosscuts the sample. Along this vein, cracks in feldspar are noticeably browner.
Magnetite (Figure XXX) in this domain are euhedral and ranges in size from 0.2mm to 10µm and displays a whitish-silver colour under PPL and is isotropic under XPL and euhedral to subhedral crystal shapes. Diamond-shaped patterns of a brighter silver streak, as described above, are dominant in many crystals.

RE06

This sample contains 57% albite, 36% blue amphibole and 6% epidote in two individual veins. The foliation is defined by the alternation of amphibole and albite domains and locally by the shape preferred orientation of blue amphibole.

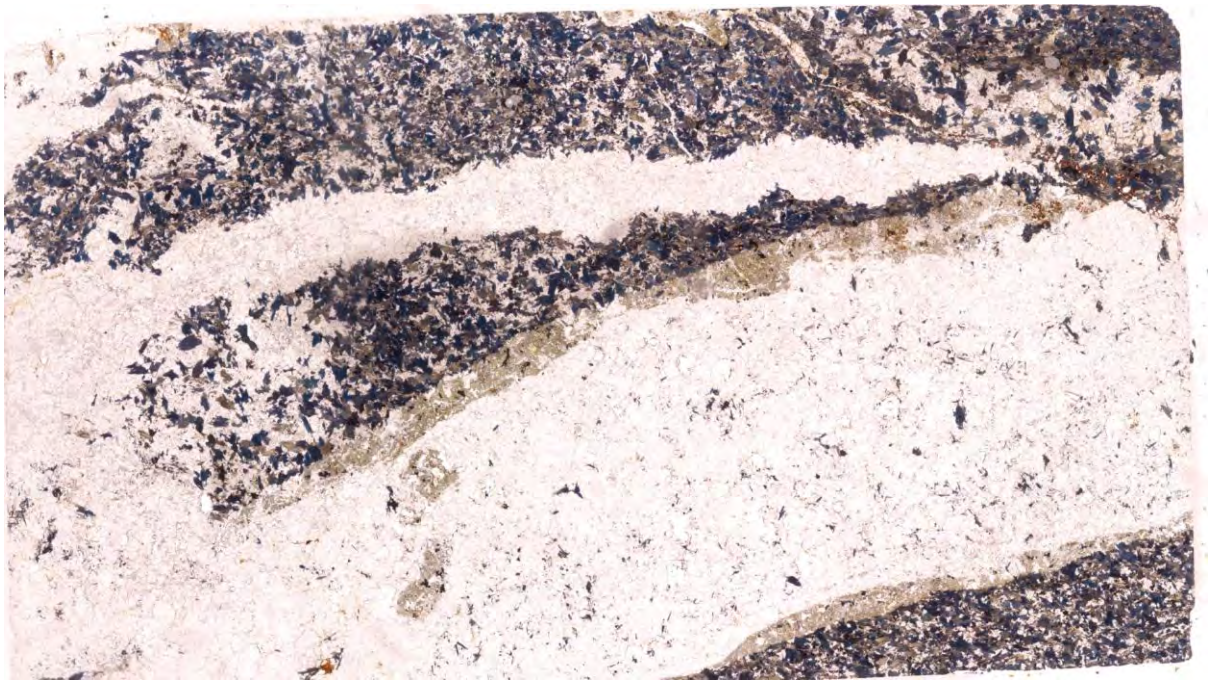

Figure 36: Full thin-section scan of the sample.

Amphibole crystal size in this sample is very uniform, with an average of around 0.3 mm. The majority of the crystals are rounded, subhedral blocks with only smaller crystals displaying blocky prismatic shapes. In PPL, amphiboles present strong, vibrant blues. In this sample, zoning between deep, vibrant blues and paler tones is clearly visible, with many crystals displaying significant pale rims. Moreover, even large crystals display a greenish tint throughout. Beyond that, crystals are clearly zoned in their inclusions, with cores often inclusion-free and only rims displaying granular titanite inclusions. Crystals that preserve larger titanites are common. Despite their usual orientation being parallel to the crystal

orientation in other samples, this sample hosts several such inclusions that are offset from it. Around 15% of amphiboles are cut perpendicular to their c-axis, and cracks are generally rare.

Epidote is a major component of this sample, with two pure epidote veins reaching up to 0.1 mm in size and displaying yellow and pinkish pleochroism in PPL. In XPL, colours are more diverse. In the thicker vein, large crystals with purely neon green colours, crystals with neon blue cores and purple rims, crystals in vibrant orange brown and crystals with pale blueish-yellow interference colours all coexist. In the thinner of the two domains, crystal sizes are generally smaller. Here, the colours described above can occur in a single crystal, with one example hosting two sets of neon-green cores that transition to purple, orange, and, finally, a thin, pale-yellow rim.

The most dominant mineral in this sample is *albite*. Crystals here are very large, some reaching 1 mm in size. Simple twinning is the most observed type in the largest crystals, followed by polysynthetic twinning. Though fine cracks with brown edges cleave through the larger crystals, the albite of this domain is overwhelmingly clear and pristine. Only a few crystals contain single, rounded grains of epidote or green amphibole needles. By contrast, blue amphibole, parallel to the foliation, is commonly intergrown with plagioclase in this domain. One decussate stilpnomelane appears to have fully replaced an amphibole.

Blue amphiboles in the plagioclase domain are generally offset from the foliation. Here, brown stilpnomelane partially replaces blue amphibole. The stilpnomelane grows in a star-shaped, decussate texture, preserving the previous amphibole prism geometry (i.e., pseudomorphically).

Magnetite displays bright greyish-silver and is often anhedral and obliterated. Crystal sizes of both range from 0.2 mm to 10µm.

RE07

This sample contains 72% amphibole, 35% magnetite, and epidote and muscovite as accessories, each below 2%. The S_2 foliation in this sample is marked by blue amphibole-rich domains alternating with albite-rich domains and by the shape preferred orientation of prismatic amphiboles from 50 µm to 0.1 mm in size. Large crystals (up to 0.3 mm in size) are oriented at high angle with respect to the dominant fabric and defined an earlier S_1 foliation. In PPL, *blue amphibole* ranges from extremely faint, pale blue to vibrant, deep blue. Zoning between the two is very common and the clearest of all the samples. The zoning patterns include patchy, vibrant cores and pale rims, as well as oscillatory zones within a single crystal. Crystals cut through the c-axis display clean core-to-rim zoning, with deep blue cores and more muted rims and a preference for titanite to be hosted in the rim rather than the core. Most of the foliation-defining crystals are inclusion-free and uncracked. The larger, rotated ones, as well as those cut through their c-axis, display some inclusions. The former commonly host a titanite in their core and granular titanites near the rim. They have a lower relief than neighbouring epidotes.

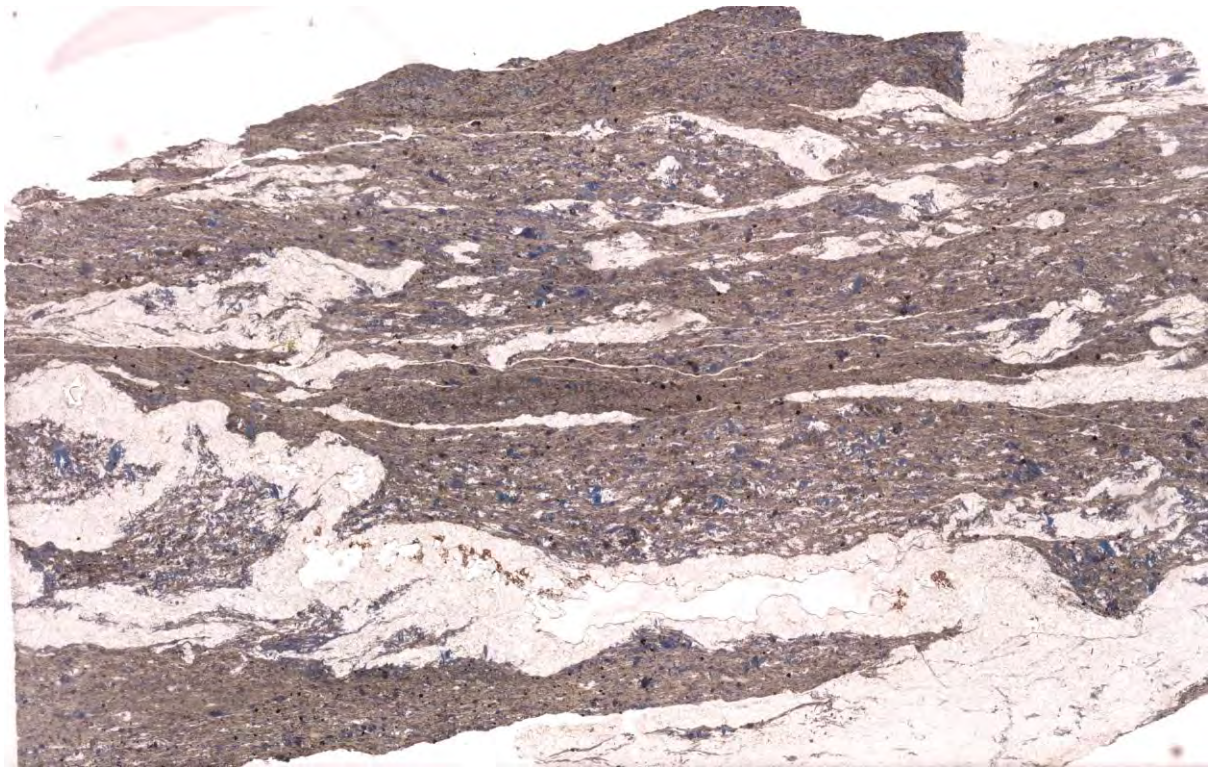

Figure 37 Thin section scan of sample RE07 (PPL).

Albite occurs in two domains, one composed largely of small crystals around 100 µm, and the other reaching up to 0.2 mm in diameter. Both domains exhibit polysynthetic twinning as well as undulose extinction. Specimens in the smaller-sized domain appear to be beginning to recrystallise. Crystals appear generally clean with only a limited number of inclusions or cracks. Near a hole in the section, larger albite grains include calcite. Only rarely are microscoping needles of green amphibole or epidote included. By contrast, swarms of blue amphibole needles and single cleaved crystals are intergrown. Despite the lack of cracks within crystals, crystal boundaries can be determined through the rimming of (XXX) along the crystal's edges.

Epidote is only a minor accessory with single scattered crystals. These crystals are 150 µm in size, commonly display cores, and are clearly zoned towards the pale-yellow rim.

Muscovite, displaying brownish-yellow colour and strong pleochroism, with deep black cleavage planes, is a common accessory mineral together with amphibole. In XPL, they display 2nd-order purple, blue, and green – like muscovite – but with too low interference colour.

RE10

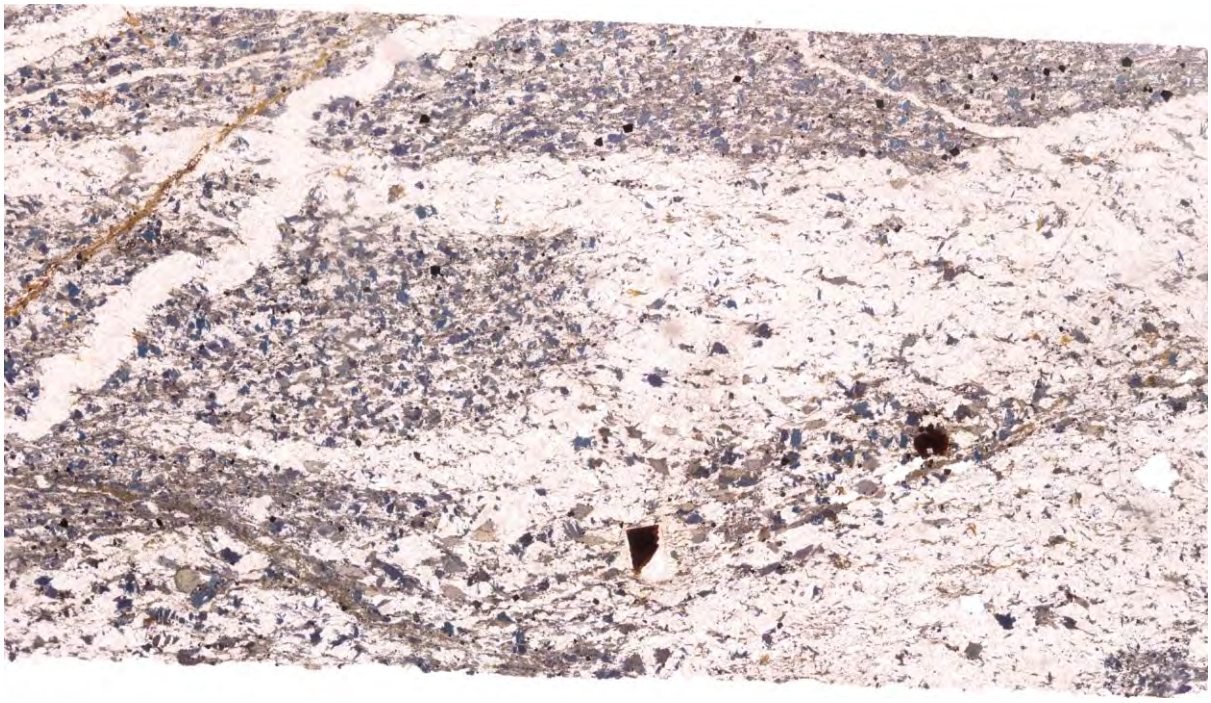

Figure 38: Thin section scan of sample RE10.

This sample contains 62% albite, 39% blue amphibole and epidote, with magnetite as an accessory below 2% each. The shape preferred orientation of blue amphiboles marks the foliation of this sample. Most crystals are rather large, reaching 0.4 mm, with the average amphibole size being 0.1 mm.. There are two domains of amphibole: in one, colours in PPL are only pale blue, without zoning into deeper tones. In the other, colours in PPL are the more common, vibrant blue. Titanite inclusions in larger amphiboles are significant, with more inclusions near the rim than in the core. Titanite inclusions in the core are also common. Moreover, needles of less-blue amphibole are included in larger crystals at random orientations. Zircon inclusions, oblique to the amphibole cleavage, are observed. Many amphiboles are heavily stilpnomelane-altered. While some crystals are fully replaced, giving the stilpnomelane a decussate, needly texture, others are not fully replaced, giving the assemblage a patchier texture.

Epidote occurs mainly in a single vein that crosscuts the sample. Here, the granular crystals are microscopic. Those slightly larger ones reach no more than 100 µm in size and are muted, brownish in XPL.

Albite ranges from only a few micrometres, if recrystallised, to up to 0.2 mm in diameter. Polysynthetic, simple and, in rare cases, tartan twinning was observed. Compared with the other samples, tartan twinning is most common here, with seven crystals displaying this feature. While recrystallised albite are mostly free from inclusions, larger crystals host a significant amount of them. Here, epidote and green amphibole are more frequently included in cores than in rims. In some crystals, oscillatory, inclusion-rich rings recording previous crystal growth phases can be observed.

Most *magnetite* crystals are 0.2 mm-sized, reddish-silver, and euhedral. They host significant inclusions at their rims. Beyond that, two massive, 2 mm-sized, silver-grey crystals of magnetite occur in this matrix. They are euhedral parts of larger, obliterated crystals which at are not hosted in this thin section.